

pubs.acs.org/JPCA Article

# Secondary Organic Aerosol Mass Yields from $NO_3$ Oxidation of $\alpha$ -Pinene and $\Delta$ -Carene: Effect of $RO_2$ Radical Fate

Published as part of The Journal of Physical Chemistry virtual special issue "Advances in Atmospheric Chemical and Physical Processes".

Douglas A. Day,\*\*,# Juliane L. Fry,\*\*,# Hyun Gu Kang, Jordan E. Krechmer, Benjamin R. Ayres, Natalie I. Keehan, Samantha L. Thompson, Weiwei Hu, Pedro Campuzano-Jost, Jason C. Schroder, Harald Stark, Marla P. DeVault, Paul J. Ziemann, Kyle J. Zarzana, Robert J. Wild, William P. Dubè, Steven S. Brown, and Jose L. Jimenez\*



Cite This: J. Phys. Chem. A 2022, 126, 7309-7330



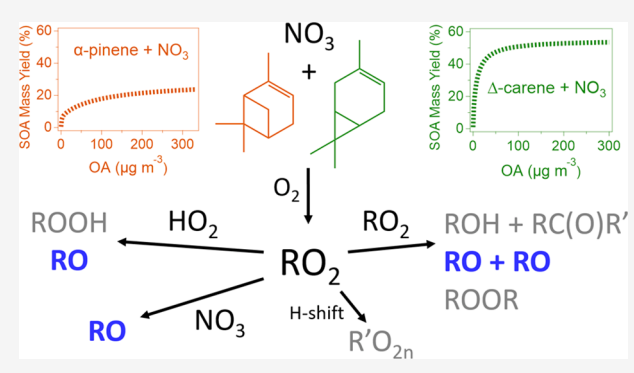
**ACCESS** 

III Metrics & More

Article Recommendations

Supporting Information

**ABSTRACT:** Dark chamber experiments were conducted to study the SOA formed from the oxidation of  $\alpha$ -pinene and  $\Delta$ -carene under different peroxy radical (RO<sub>2</sub>) fate regimes: RO<sub>2</sub> + NO<sub>3</sub>, RO<sub>2</sub> + RO<sub>2</sub>, and RO<sub>2</sub> + HO<sub>2</sub>. SOA mass yields from  $\alpha$ -pinene oxidation were <1 to ~25% and strongly dependent on available OA mass up to ~100 μg m<sup>-3</sup>. The strong yield dependence of  $\alpha$ -pinene oxidation is driven by absorptive partitioning to OA and not by available surface area for condensation. Yields from  $\Delta$ -carene + NO<sub>3</sub> were consistently higher, ranging from ~10–50% with some dependence on OA for <25 μg m<sup>-3</sup>. Explicit kinetic modeling including vapor wall losses was conducted to enable comparisons across VOC precursors and RO<sub>2</sub> fate regimes and to determine atmospherically relevant yields. Furthermore, SOA yields were similar for each monoterpene across



the nominal RO<sub>2</sub> + NO<sub>3</sub>, RO<sub>2</sub> + RO<sub>2</sub>, or RO<sub>2</sub> + HO<sub>2</sub> regimes; thus, the volatility basis sets (VBS) constructed were independent of the chemical regime. Elemental O/C ratios of ~0.4–0.6 and nitrate/organic mass ratios of ~0.15 were observed in the particle phase for both monoterpenes in all regimes, using aerosol mass spectrometer (AMS) measurements. An empirical relationship for estimating particle density using AMS-derived elemental ratios, previously reported in the literature for non-nitrate containing OA, was successfully adapted to organic nitrate-rich SOA. Observations from an NO<sub>3</sub><sup>-</sup> chemical ionization mass spectrometer (NO<sub>3</sub>– CIMS) suggest that  $\Delta$ -carene more readily forms low-volatility gas-phase highly oxygenated molecules (HOMs) than  $\alpha$ -pinene, which primarily forms volatile and semivolatile species, when reacted with NO<sub>3</sub>, regardless of RO<sub>2</sub> regime. The similar  $\Delta$ -carene SOA yields across regimes, high O/C ratios, and presence of HOMs, suggest that unimolecular and multistep processes such as alkoxy radical isomerization and decomposition may play a role in the formation of SOA from  $\Delta$ -carene + NO<sub>3</sub>. The scarcity of peroxide functional groups (on average, 14% of C<sub>10</sub> groups carried a peroxide functional group in one test experiment in the RO<sub>2</sub> + RO<sub>2</sub> regime) appears to rule out a major role for autoxidation and organic peroxide (ROOH, ROOR) formation. The consistently substantially lower SOA yields observed for  $\alpha$ -pinene + NO<sub>3</sub> suggest such pathways are less available for this precursor. The marked and robust regime-independent difference in SOA yield from two different precursor monoterpenes suggests that in order to accurately model SOA production in forested regions the chemical mechanism must feature some distinction among different monoterpenes.

# 1. INTRODUCTION

Secondary organic aerosol (SOA) produced from the reaction of volatile organic compounds (VOC) and atmospheric oxidants is a major component of the global aerosol burden. <sup>1-4</sup> SOA impacts global as well as local radiative balance and climate forcing. <sup>5,6</sup> Furthermore, SOA contributes to particulate matter (PM), which represents a major health risk factor globally and is known to increase the likelihood of cardiovascular disease, respiratory disease, and death. <sup>8</sup> These

Received: June 26, 2022 Revised: September 10, 2022 Published: September 28, 2022





adverse health effects of air pollution also incur financial costs. 9,10

A large fraction of VOC emissions is biogenic,  $^{11}$  and consequently, a large fraction of SOA originates from biogenic hydrocarbons.  $^{12}$  Monoterpenes constitute  $\sim 15\%$  of BVOC emissions by mass.  $^{13}$  Studies suggest that the emission of BVOC will rise due to a variety of factors, including a warming climate.  $^{14-16}$  The rise in BVOC emissions increases the potential for SOA formation,  $^{15}$  because monoterpenes generally produce large amounts of SOA when oxidized by nitrate radical (NO<sub>3</sub>), ozone (O<sub>3</sub>), or hydroxyl radical (OH), as well as producing lower-volatility SOA.  $^{17}$ 

The high reactivity of  $NO_3$  with alkenes and their large SOA yields has drawn increasing attention. <sup>18</sup> Pye et al. <sup>19</sup> found that the inclusion of  $NO_3$  reactions into GEOS-Chem doubles the SOA predicted to be produced from monoterpenes in the United States and that  $NO_3$  chemistry would account for a small contribution ( $\sim$ 5%) of SOA on a global scale. However, an Oslo CTM2 model study by Hoyle et al. <sup>20</sup> found that  $NO_3$  oxidation products could be responsible for 21-27% of global SOA. Measurements from the Southern Oxidant and Aerosol Study (SOAS) suggest that  $NO_3$ -initiated oxidation products are a major portion of organic particulate matter. <sup>21,22</sup> Another study by Pye et al. <sup>23</sup> used CMAQ and found that including the aerosol partitioning of gas-phase organic nitrates in the model improved organic aerosol (OA) predictions during SOAS.

 $\alpha$ -Pinene is the most abundant biogenic monoterpene globally, <sup>13</sup> but previously measured SOA mass yields from its NO<sub>3</sub> oxidation are inconsistent, ranging from 0 to 25%. <sup>24–31</sup> This latter and highest yield was found at low temperature, 5 °C, and >100  $\mu$ g m<sup>-3</sup> background OA. The generally lower SOA mass yields from  $\alpha$ -pinene + NO<sub>3</sub> are in stark contrast with the higher values from reaction of NO<sub>3</sub> with other monoterpenes. <sup>18</sup>

A potential explanation for these discrepancies is the varying concentrations of reactants used in those experiments. Historically, chamber experiments used higher VOC and oxidant concentrations than found in the atmosphere in part due to the difficulty of analyzing very small amounts of SOA. Recently, however, some chamber studies have focused on achieving more atmospherically relevant conditions. While much attention has gone to mimicking atmospheric concentrations in experiments, until recently, less has been paid to another potentially important factor of atmospheric relevance in monoterpene + NO $_3$  studies: the organic peroxy radical (RO $_2$ ) lifetime and fate.

The RO<sub>2</sub> fate has been identified as a crucial step in forming low volatility gas phase products for some chemical systems.<sup>32–36</sup> Kirchner and Stockwell<sup>37</sup> suggest that either RO<sub>2</sub> + NO<sub>3</sub> or RO<sub>2</sub> + RO<sub>2</sub> is the major RO<sub>2</sub> loss pathway in the nighttime urban environment. Ziemann and Atkinson<sup>33</sup> note that under nighttime conditions when NO concentrations are sufficiently low, RO2 + HO2 may dominate over RO2 + RO<sub>2</sub>. Mao et al.<sup>38</sup> found nighttime ambient concentrations of  $\mathrm{HO}_2$  to be  $\sim\!5$  pptv at a ponderosa pine plantation, which highlights that RO<sub>2</sub> + HO<sub>2</sub> may be an important pathway in the ambient nighttime atmosphere. Unfortunately, most previous experiments studying BVOC + NO<sub>3</sub> generally did not consider RO<sub>2</sub> + HO<sub>2</sub> reactions, although a few recent studies have.<sup>29,31,39-41</sup> Recent work has reopened the question of the products of the RO<sub>2</sub> + RO<sub>2</sub> reactions, showing that the rates of formation of dialkyl peroxides (ROOR), which have been previously assumed negligible, are in fact rapid for several

RO<sub>2</sub> radicals produced from the OH radical initiated oxidation of 1,3,5-trimethylbenzene. Because these ROOR products have substantially lower volatility relative to their precursors, this reaction pathway can rapidly lead to condensable products. Additional recent work in the NO<sub>3</sub> + β-pinene and Δ-carene systems has shown that RO<sub>2</sub> + RO<sub>2</sub> gas-phase reactions in combination with particle-phase oligomerization can underpin large SOA mass yields from monoterpenes. Recent work on the NO<sub>3</sub> + α-pinene system probing RO<sub>2</sub> fate dependence showed large yields under certain conditions, which they attributed to dominance of RO<sub>2</sub> + RO<sub>2</sub> reactions, with an estimated SOA mass yield of ~65% for that pathway and negligible SOA for other RO<sub>2</sub> fates. The substantial sub

Given the uncertainties in atmospheric  $RO_2$  fate, we examine how these different fates affect SOA formation from  $NO_3$  oxidation of terpenes. Specifically, we sought to determine if the observed anomalously low  $\alpha$ -pinene SOA yield was unique to particular  $RO_2$  fates or chamber artifacts, by performing experiments across three different putative  $RO_2$  fates,  $RO_2$  +  $NO_3$ ,  $RO_2$  +  $RO_2$ , and  $RO_2$  +  $RO_2$ , and using a range of inorganic and organic seed aerosol concentrations (Figure 1).

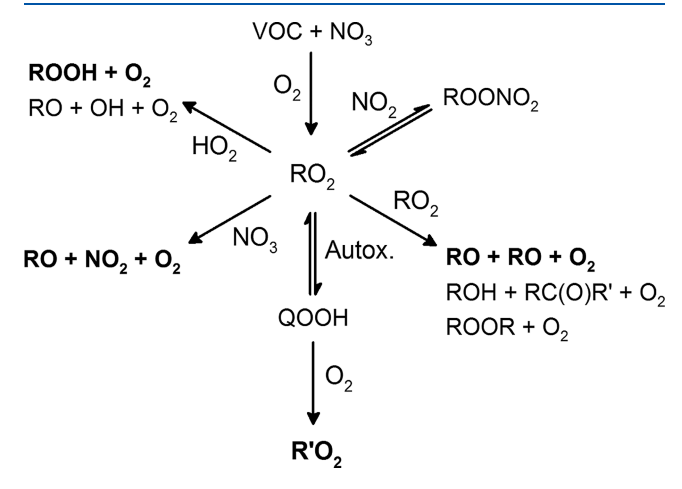


**Figure 1.** Oxidation of α-pinene or  $\Delta$ -carene by NO<sub>3</sub> radical yields a peroxy radical (RO<sub>2</sub>), which has multiple subsequent reactive fates that are targeted in this study by variations in initial concentrations of VOC, N<sub>2</sub>O<sub>5</sub>, and HCHO.

We chose to compare  $\alpha$ -pinene to  $\Delta$ -carene because these provide a good contrast. Both have similar endocyclic double-bond environments, but  $\Delta$ -carene displays much higher SOA yields. We also investigate the chemical composition of the gases and aerosol under this wide range of conditions to help discern the processes and conditions that control SOA formation.

# 2. EXPERIMENTAL METHODS

**2.1.** Laboratory Chamber Facility, Instrumentation, and Methods. During the summer of 2014, experiments were conducted in a 7 m³ FEP Teflon environmental chamber at the CU-Boulder Environmental Chamber facility. <sup>46</sup> In the summer of 2015, experiments were conducted in a 20 m³ FEP Teflon chamber in the same facility. <sup>47</sup> Most experiments were carried out under dry (<2% relative humidity (RH)) conditions, except for four under elevated RH where organic nitrate hydrolysis was investigated. The chambers were at room temperature (21–23 °C) in dark enclosures. A diagram of the instrumentation used is shown in Figure \$1.

 $N_2O_5$  was injected by flowing dry zero air (100–250 standard cubic centimeter per minute, sccm) through a trap of  $N_2O_5$  crystals held at a constant, adjustable temperature (–60 to –25 °C) via a heated sleeve immersed in isopropanol and dry ice. The  $N_2O_5$  within the chamber was monitored with an  $NO_3/N_2O_5$  cavity ring-down spectrometer. A relative humidity probe, chemiluminescent  $NO_x$  analyzer (Thermo 42i-TL), and an  $O_3$  analyzer (2014: Teledyne API T400; 2015: Thermo 49i) monitored the chamber air continuously during both experiment series. A commercial  $CO_2/CO/CH_4/H_2O$  cavity ring-down spectrometer (Picarro G2401) was used to measure  $CO_2$  that was coinjected with the terpene, in order to compute chamber volume during extended multi-injection experiments conducted in 2015.

A known volume of  $\alpha$ -pinene (98%, CAS no. 80–56–8, Aldrich) or  $\Delta$ -carene (90%, CAS no. 13466–78–9, Aldrich; 99%, CAS no. 498-15-7, Aldrich) was injected into a sealed round-bottomed flask with a microsyringe or electronic pipette and gently heated ( $\sim$ 40 °C) with N<sub>2</sub> or N<sub>2</sub>/CO<sub>2</sub> gas flowing through the flask to introduce the VOC to the chamber. Formaldehyde was similarly heated and flowed into the chamber by gently heating paraformaldehyde (96%, CAS no. 30525-89-4, Acros Organics) contained in a glass bulb using a heat gun until the solid is fully sublimated. The  $\Delta$ -carene used in 2014 was a mixture of enantiomers (one of which is not commonly found in nature), while that used in 2015 was the more commonly observed enantiomer in nature (see discussion in Supporting Information section S1.0, Figure S2). Additionally, it was observed that the  $\Delta$ -carene used in 2014 contained some impurities that led to nonreactive aerosol growth which was separated using AMS measurements (see section S1.2.1). A gas chromatography flame ionization detector (GC-FID, Hewlett-Packard; 2014 experiments) and a proton transfer reaction quadrupole mass spectrometer (PTR-MS, Ionicon; 2015 experiments) were used to measure the concentration of monoterpene in the chamber. Gas samples for GC-FID analysis were collected by pulling chamber air through glass sampling tubes holding Tenax TA sorbent (at 0.250 sccm for 10 min, immediately following 20 min of stainless-steel sampling tubing conditioned with chamber air) and later analyzed by GC-FID, as described in Algrim and Ziemann. 50 Calibrations for the Tenax/GC-FID and PTR-MS were constructed by adding measured amounts of  $\alpha$ -pinene and  $\Delta$ -carene into the chamber (of known volume), in the absence of reactants. The chamber bag volumes were measured by injection of known amounts of CO<sub>2</sub>, and measured after mixing. For the 7 m<sup>3</sup> chamber used in the 2014 experiment series, this was done for the nominal full size, which was applicable to all 2014 experiments. For the 20 m<sup>3</sup> chamber used in the 2015 experiments, CO<sub>2</sub> injections were conducted during most VOC injections, including all where VOC injections occurred following extended sampling, associated with decreasing bag volume.

A scanning mobility particle sizer (SMPS, TSI models: 3080 electrostatic classifier, 3081 differential mobility analyzer, and 3010 (2014)/3775 (2015) condensation particle counter) and a high-resolution time-of-flight aerosol mass spectrometer (HR-ToF-AMS, hereafter AMS, Aerodyne Inc.)<sup>51,52</sup> were used to characterize the particle size distributions (volume, surface area, and number concentrations) and chemical composition, respectively. The aerosol sample flow was dried to <30% RH using a Nafion drier during elevated humidity experiments. Mass spectra, concentrations, and size distributions of aerosol

composition measurements collected with the AMS were analyzed with standard ToF-AMS analysis software packages (Squirrel version  $\geq 1.56D$  and PIKA version  $\geq 1.15D$ ). 51,53The AMS sensitivity was calibrated by conducting weekly calibrations with monodisperse 400 nm dried ammonium nitrate aerosol and the "fragmentation table" was adjusted based on daily aerosol-free sampling (via a HEPA filter or prior to experiments after overnight flushing of the chamber). AMS size distributions were calibrated using polystyrene spheres (PSLs, 70-900 nm), and the SMPS sizing was checked with PSLs (confirmed within 2% of recorded sizing). Relative ionization efficiencies (RIE) for ammonium and sulfate were determined by sampling ammonium nitrate and ammonium sulfate test aerosol. All aerosol concentrations are reported in Boulder, CO ambient pressure and laboratory temperature ( $\sim$ 830 mbar,  $\sim$ 20 °C).

The average RIE of SOA produced from NO<sub>3</sub> + terpene oxidation was determined to be 2.36 (plausible range: 2.00-2.86), based on comparisons to SMPS integrated volume and estimated density using OA elemental ratios and comparisons of AMS and SMPS size distributions, with a collection efficiency of 0.875 (relevant to pure SOA only; plausible range: 0.75-1.00) when sampling pure SOA. See section \$1.1 for details and discussion of that analysis. The RIE applied for terpene SOA is nearly double that typically applied for ambient OA quantification (1.4). 52,54,55 The application of the RIE for SOA affects the organic nitrate/SOA ratios (section 3.1), SOA yields in cases where ammonium sulfate or organic (DOS) seed was present, and elemental ratios when DOS seed was present. Elemental ratios (O/C, H/C) were determined according to the method described in Canagaratna et al.<sup>56</sup> to compute the ratios for the "AMS organics" component as is routine for AMS, but then also including the oxygen from organic nitrate functional groups (measured as NO<sup>+</sup> and NO<sub>2</sub><sup>+</sup> in the AMS spectrum) for the complete O/C of the SOA (section S1.1). All nitrate measured with the AMS was assumed to be in organic nitrate functional groups (hereafter pRONO<sub>2</sub>), except for the four humidified experiments when substantial ammonium nitrate may have formed. For those experiments, nitrate was apportioned between organic and inorganic nitrate using the observed NO2+/NO+ ion ratios in the AMS spectrum, to refine the quantification of pRONO<sub>2</sub>, <sup>57</sup> with details specific to this data set. 58 The RIE for organic nitrate was assumed to be the same as that measured for ammonium nitrate.

The gaseous organic compounds were studied with a high-resolution time-of-flight chemical ionization mass spectrometer (NO $_3$ –CIMS, Aerodyne) during select experiments (2015 only). The CIMS sampled directly adjacent to the Teflon reaction bag within the chamber enclosure to minimize sampling losses. The nitrate ion source enables measurements of semivolatile and low-volatility oxidized organic compounds in the gas-phase, and the "inletless" source design<sup>46,59</sup> has sufficiently short residence time and flow characteristics to reduce diffusive losses to source walls, enabling the NO $_3$ –CIMS to measure nonvolatile compounds with relatively minimal losses (35%) to inlet walls. Concentrations of HOMs were calibrated according to the methods described in Krechmer et al.<sup>46</sup>

**2.2. Experiment Overview.** Details on individual experiments are available in Tables S1 and S2. For the  $RO_2 + NO_3$  experiments,  $N_2O_5$  was injected into the chamber until  $\sim 100$  ppb was reached, which was then followed by the injection of

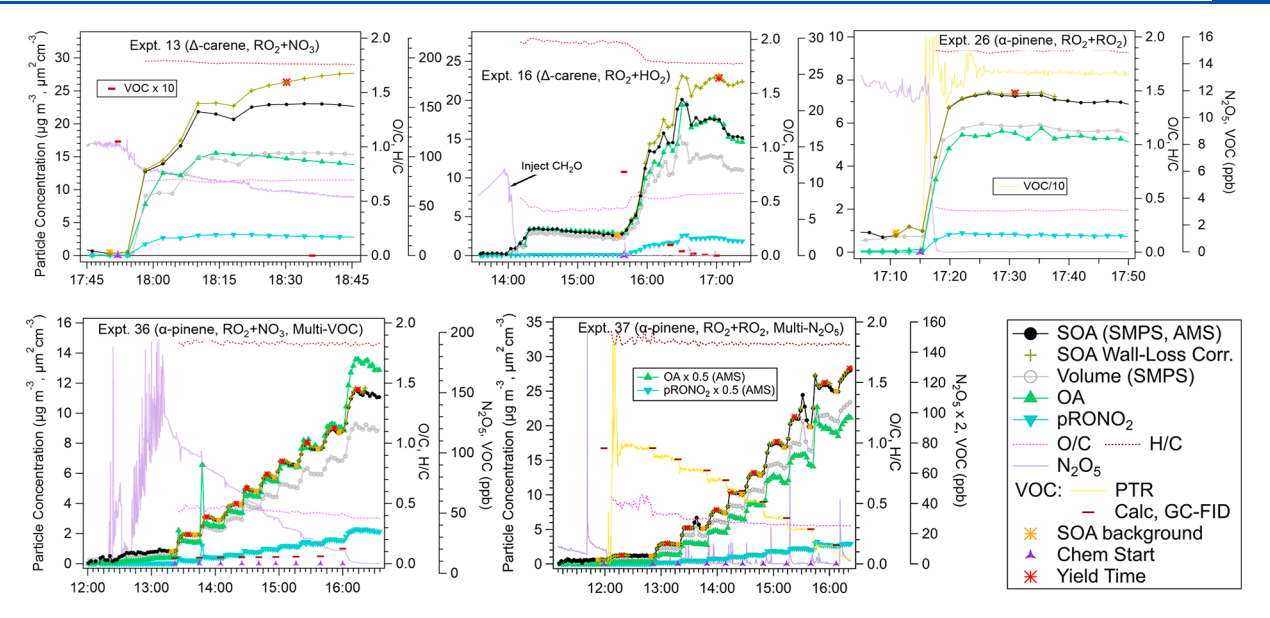


Figure 2. Representative experimental time series showing different terpene precursors,  $RO_2$  regime targets, and VOC/oxidant injection sequences. Single-injection experiments and ones with multiple serial  $N_2O_5$  or VOC injections are shown. All fundamental measurements for the yield and composition measurements reported in this analysis are shown. VOC concentrations include those directly measured by PTR or GC-FID and/or those calculated from individual quantitative injections. None of the experiments shown include particle seed injections; therefore, SOA computed from SMPS measurements (using AMS-derived density) are equivalent to total OA. See Figure S11 for an example time series of particle concentrations for a single-injection  $RO_2 + RO_2$  regime  $\Delta$ -carene experiment and Tables S1 and S2 for additional individual experiment details. The spiky nature of the  $N_2O_5$  and VOC time series during some periods is due to injections of those compounds causing brief periods of incomplete mixing before stabilization (of the excess reagent) and/or complete consumption (of the limiting reagent), not instrument measurement noise. Those on-line measurements during such periods were not directly used in yield calculations and are only shown here to illustrate the observables for typical experiments.

~10 ppb of the VOC. Similarly, ~10 ppb of  $N_2O_5$  was introduced to the chamber prior to the injection of  $\sim$ 100 ppb of VOC for the RO<sub>2</sub> + RO<sub>2</sub> experiments. In RO<sub>2</sub> + HO<sub>2</sub> experiments, formaldehyde (HCHO) was injected into the chamber by heating an amount of paraformaldehyde expected to produce ~50 ppm of HCHO in the chamber, followed by a continuous flow of  $N_2O_5$  to form  $HO_2$  (CH<sub>2</sub>O +  $NO_3$   $\rightarrow$  $HNO_3 + CO + HO_2$ ) and injection of the VOC (~10 ppb). During the 2014 experiments, a Teflon-coated fan was run for 15-60 s during initial injection of the VOC, again immediately after VOC injection completed and also every 10-15 min during continuous  $N_2O_5$  injection (RO<sub>2</sub> + HO<sub>2</sub> experiments). During the 2015 experiments, the fan was run for 15 s every 120 s (on an automatic timer) during VOC and N<sub>2</sub>O<sub>5</sub> injections. For seeded experiments, dioctyl sebacate (DOS) or ammonium sulfate (NH<sub>4</sub>SO<sub>4</sub>) particles were added to the chamber prior to the introduction of reactants using a custom evaporation/condensation particle generator<sup>60</sup> or Colison atomizer (TSI model 3076), respectively. Similarly, pure water (Milli-Q) was gently heated outside the chamber and then introduced until a desired RH was reached for high-RH experiments. In some instances, multiple injections of VOC or N<sub>2</sub>O<sub>5</sub> were conducted after the initial reactions, resulting in multiple yield measurements.

**2.3. SOA Yields and Characterization.** SOA yields were measured using the integrated volume calculated from the SMPS, density estimated from the AMS composition, and VOC reacted. The aerosol volume measured by the SMPS was corrected for wall losses with wall loss coefficients specific to the chamber for each experiment (wall loss measurements are shown in Figure S3 for each chamber). These wall losses were determined using integrated volume concentrations of all particle size distributions from 45 to 120 min periods during

which the chamber contained only either dioctyl sebacate (DOS) organic seed or ammonium sulfate seed with a small contribution of completely reacted  $\Delta\text{-}carene$  SOA, with all instruments sampling and the bag at a similar volume range to the experiments. The chamber fan was on for a duty cycle similar to that of the SOA experiments. The resulting size-independent first-order wall loss rate constants assumed a continuously stirred tank reactor. The SMPS integrated volume concentrations were corrected for inlet and line losses (typically on order of  $\sim\!5\%$  of volume) using the Particle Loss Calculator.  $^{61}$ 

Because SOA formation occurs relatively rapidly when initiated by NO<sub>3</sub> sourced from N<sub>2</sub>O<sub>5</sub> dissociation, wall losses of aerosols were not generally expected to exert a large effect on SOA mass yields measured in these experiments. However, wall losses of semivolatile vapors may affect measured yields in some cases,<sup>47</sup> particularly when longer reaction times are explored. While the RO<sub>2</sub> + NO<sub>3</sub> and RO<sub>2</sub> + RO<sub>2</sub> experiments conducted here featured rapid aerosol growth (peak reached in  $\sim 10$  min), the growth was slower in the RO<sub>2</sub> + HO<sub>2</sub> experiments (~50 min), resulting in particle and semivolatile vapor wall loss corrections being more important in the latter. Additionally, wall losses of vapors may be more important for experiments where there is little aerosol present to facilitate efficient gas-to-particle partitioning, such as nonseeded  $\alpha$ pinene experiments which typically showed little to no new particle formation. Figure 2 shows the time series of aerosol components of some typical experiments in each regime to illustrate this difference in timing. Typical wall loss corrections for particle-to-wall transfer were <10% (10-45%) for 2015 (2014) experiments (Figure S4). Because of the wide variety of experimental conditions explored in this study, and the likely variability of these aerosol and semivolatile vapor wall losses

across experiments, we undertook explicit kinetic modeling of semivolatile vapor-phase wall loss processes for each experiment, as described in section 2.4.

Aerosol mass yields were calculated by converting the wallloss-corrected SMPS aerosol volume concentration to aerosol mass concentration ( $\mu g \text{ m}^{-3}$ ) using density estimated from the composition of the SOA as measured by the AMS. The standard approach to estimating density with AMS uses only the O/C and H/C elemental ratio and an empirically developed relationship. 62 However, since that relationship was developed with non-nitrate-containing standards and SOA, here we tested including the oxygen and nitrogen atoms from the organic nitrate together with the standard AMS-derived O/ C in the Kuwata et al. e1 relationship. Results were compared to independently derived density, using comparison of the AMS particle time-of-flight (PToF) vacuum aerodynamic diameter to SMPS-measured mobility diameter<sup>51</sup> for several experiments (nonseeded experiments with adequate PToF signal-to-noise). Results were consistent within 10%, thus supporting the application of this revised density calculation to all experiments here (and further supporting use of this revised density estimation for nitrate-rich SOA in general; see section S1.1.2 for details).

We reproduce the adapted equation here (developed and shown as eq S4 in the Supporting Information), for greater accessibility and to encourage its general use:

$$\rho_{\rm org} = \frac{12 + 1({\rm H/C}) + 16(({\rm O+N})_{\rm T}/{\rm C})}{7.0 + 5.0({\rm H/C}) + 4.15(({\rm O+N})_{\rm T}/{\rm C})} \times {\rm KFC}$$

where  $ho_{
m org}$  is the particle density of the organic components in g cm<sup>-3</sup>, H/C and  $(O+N)_T/C$  represent the molar elemental ratios of AMS organic, and (O+N)<sub>T</sub> includes the contribution of O from standard AMS organic elemental ratios analysis summed with the O and N from the organic nitrate functional group concentrations (see Day et al.<sup>57</sup> for methods for separating organic/inorganic nitrate). Only two of the oxygens per organic nitrate functional group are added, since one O from nitrate is expected to be retained on the carbon backbone and included in the standard AMS O/C analysis. Finally, the KCF is an experimentally determined coefficient, which for this study was determined to be 1.08. In the absence of independent evidence for the organic aerosol under study, we recommend using that value determined here (1.08), or simply setting it to 1. Use of this adapted and empirically constrained equation resulted in an increase of ~20% in particle density for most experiments, compared to using only O/C from standard AMS elemental ratio analysis (for the SOA here with O/C, excluding pRONO<sub>2</sub> contributions, of 0.3–0.45 and pRONO<sub>2</sub>/SOA of ~0.15). Thus, for this range of O/C values (which is fairly typical of ambient OA and laboratorygenerated SOA), underestimation of density of order the pRONO<sub>2</sub>/SOA mass ratio would be expected. For many ambient measurements, where pRONO<sub>2</sub>/SOA is only a few percent, this would be insignificant, while for other sites where fractions are larger, it may become significant. See Figure 5b in Ng et al. 18 for a survey of ambient organic nitrate contributions, noting that the values reported there are for the total organic nitrate molecule contribution (MW 200-300 g mol<sup>-1</sup> assumed range for different studies), which can be computed as  $(200-300)/62 \times pRONO_2/OA$ . Likewise for chamber-generated aerosol, similar considerations should be made in estimating particle densities using elemental ratios,

which will likely be applicable for studies including  $NO_3$  radical oxidation and sometimes high- $NO_x$  photooxidation where substantial nitrate is formed.

SMPS volume measurements were used to calculate yields and total OA concentration, instead of using AMS concentrations, due to uncertainties related to collection efficiency, relative ionization efficiency, and overall calibration. When ammonium nitrate seed, DOS seed, or contaminant from the  $\Delta$ -carene used in the 2014 studies was present, the density, mass concentrations, and elemental ratios and nitrate contribution of SOA was separated from the other components using the AMS measurements (see Supporting Information section \$1.2). The densities of SOA formed at the times when SOA yields were computed ranged 1.08–1.53 g cm<sup>-3</sup> for  $\alpha$ pinene experiments and 1.22-1.48 g cm<sup>-3</sup> for  $\Delta$ -carene experiments (see Figure S6). DeVault and Ziemann<sup>44</sup> reported a density of 1.26  $\pm$  0.07 g cm<sup>-3</sup> for SOA generated from NO<sub>3</sub> +  $\Delta$ -carene, based on functional group analysis and application of a similar approach using elemental ratios (treating N the same as O), based on the Kuwata et al.<sup>62</sup> equation.

The  $\Delta M_{\rm aero}$  values were calculated by subtracting any preexisting aerosol mass at the time of VOC injection from the aerosol mass at the time  $\Delta VOC$  was measured. The  $\Delta VOC$ was determined using a few different approaches, depending on the order and relative amounts of reactants added. When N<sub>2</sub>O<sub>5</sub> was injected into the chamber first and followed by VOC injection, and one reactant was in large excess (nominal RO<sub>2</sub> +  $RO_2$  and  $RO_2 + NO_3$  experiments), the limiting reagent was used to determine the amount of VOC reacted. Thus, when  $N_2O_5 > VOC$  (e.g., nominal  $RO_2 + NO_3$  experiment), the full amount of VOC injected was taken as  $\Delta$ VOC, while when  $VOC > N_2O_5$  (e.g., nominal  $RO_2 + RO_2$  experiment), the amount of N2O5 present in the chamber prior to reaction (measured with CRDS and observed to fully react) was taken as  $\Delta VOC$ . For excess  $N_2O_5$  experiments, in the absence of VOC measurements, complete reaction of the VOC could always be confirmed by observation of N2O5 remaining following reaction. In the cases where reactants were similar in concentration, the amount of remaining VOC at the recorded yield time was measured (with Tenax/GC-FID or PTR-MS) and subtracted from the initial VOC concentration injected to compute  $\Delta$ VOC. For experiments where VOC was added first to the chamber and then N2O5 was added as a continuous injection (typically at a rate not precisely known), the observed decrease in VOC was taken as  $\Delta$ VOC (e.g., nominal RO<sub>2</sub> + HO<sub>2</sub> experiments or the multistep experiments conducted during 2015 where sequential additions of N<sub>2</sub>O<sub>5</sub> were added to excess VOC). For the experiments where VOC was added as sequential steps to excess N2O5 during 2015, the same approach as described above, for when N<sub>2</sub>O<sub>5</sub> is added first, was applied. The resulting SOA mass yield values (Y = $\Delta M_{\rm aero}/\Delta {\rm VOC}$ ) are shown in Table S1. Further details on the methods used to separate the SOA concentrations from the particle seed concentrations (i.e., ammonium sulfate, DOS) for the yield calculations are provided in section S1.2.

The presence of impurities in the  $\Delta$ -carene was detected when  $\sim$ 1000 ppb of  $\Delta$ -carene were added to the chamber in a preliminary experiment and exceedingly high and unrealistic apparent aerosol yields were observed. Injection of the VOC in the absence of oxidants confirmed that the contaminant partitioned to the aerosol without chemical reaction. Consequently, all following RO<sub>2</sub> + RO<sub>2</sub> regime experiments were conducted with lower excess VOC concentrations than

initially planned (100 instead of 1000 ppb), and any additional aerosol mass from the impurity partitioning to aerosol for those experiments was removed prior to yield calculations and chemical characterization of SOA by positive matrix factorization (PMF) of the AMS spectra (see section S1.2). The 1000 ppb experiment was not used in the yield and composition analysis here. Select experiments were repeated with higher purity  $\Delta$ -carene during 2015 with no significant differences in SOA mass yields or composition observed.

2.4. Compound Fate Modeling of Semivolatile Vapor Wall Losses. In order to assess the effects of losses of semivolatile vapors to chamber walls and estimate correction factors for SOA yields (and VBS parameters derived from yield curves), individual experiments were modeled according to the framework applied in Krechmer et al.<sup>47</sup> and Liu et al.<sup>63</sup> The key processes tracked by the kinetic model include the following: (1) formation of compound classes in three volatility bins from reaction of the terpene ( $\alpha$ -pinene or  $\Delta$ carene) with nitrate radical, (2) condensation of gases to particles, (3) evaporation of compounds from particles, (4) condensation of gases to chamber walls, (5) evaporation of compounds from chamber walls, and (6) irreversible particle loss to chamber walls. See Liu et al. 63 for an analogous schematic of the key processes for alkanol photooxidation (their Supporting Information Figure 1). It is critical to capture the dynamics of these processes to properly assess the effects on yields, since the entire system is never in equilibrium, as the interplay between the different processes continually evolves. That evolution is driven, in part, by the wide range of time constants involved for the different processes. For example, for these experiments, SOA-forming reaction products are produced on time scales of seconds to minutes, and gasparticle partitioning occurs on the scale of minutes to tens of minutes. Gas-wall exchange has time scales of tens of minutes to an hour, and particle-wall loss time scales are several hours. Moreover, several of the processes depend on compound volatility and dynamic parameters (e.g., organic absorbing mass concentration). Generally, SOA yields were calculated during a period when aerosol concentrations peaked, signifying that rapid gas-phase chemistry had waned, gas-particle partitioning was in pseudoequilibrium, and particle and vapor losses were not yet dominant in aerosol mass concentration dynamics. However, even under those conditions, chamber wall effects can already be substantial. Moreover, there were substantial differences in the conditions and sequences of some experiments such as the presence/absence of seed or rapid newparticle formation, serial oxidation steps for some  $\alpha$ -pinene/ NO<sub>3</sub> experiments, or longer reactions times required for the "RO<sub>2</sub> + HO<sub>2</sub> regime" experiments (see Figure 2). Therefore, modeling the vapor fate was not only critical to compute accurate yields but also to enable direct comparison across VOC precursors and RO2 fate regimes.

The compound fate modeling was conducted using KinSim software (v4.08) within Wavemetrics Igor Pro  $8.^{64}$  Inputs for all model runs included the initial terpene and  $N_2O_5$  concentrations (or  $N_2O_5$  injection rate), time-dependent organic aerosol (OA) mass concentrations, and particle condensational sink (CS) rate. The mechanism is shown in Table S4. CS and OA are fully constrained by the experimentally measured time series. Sources and derivations of coefficients for the reactions and phase partitioning used in the mechanism are described in section S1.3. Since the calculated yields already accounted for particle-wall loss, the

aim of the modeling was to compare yields calculated with and without gas-wall interactions included, with the former taken to represent the conditions under which yields were measured in the chamber (with standard particle-wall loss corrections) and the latter to be representative of the "true yield" as expected for the atmosphere. The ratio of the SOA formed without to with gas-wall effect is termed  $\Phi$ , as described in Krechmer et al.<sup>47</sup> Values here, for all experiments and cases considered, ranged from 0.65-5.5 and can be applied multiplicatively as the yield correction factor.  $\Phi$  was always computed for the time point in the experiment corresponding to when the standard yield calculations were done. Figure S11 shows examples of time series of modeled compound fates for typical  $\Delta$ -carene and  $\alpha$ -pinene experiments, with and without vapor interactions with chambers walls. Table S5 outlines the five vapor wall loss modeling cases.

An iterative process was conducted to solve for consistent sets of  $\Phi$ , yields, and volatility basis set (VBS) parameters for both chemical systems (i.e.,  $\Delta$ -carene/NO<sub>3</sub>,  $\alpha$ -pinene/NO<sub>3</sub>). In practice, each iterative cycle involved the following: (1) fitting the yield curve (cf. Figure 4) to compute the VBS, (2) using that VBS in the compound fate modeling, to derive  $\Phi$  for each experiment, and (3) applying those  $\Phi$  to correct the initial experimentally determined yields. Then the cycle was repeated with step 1 but now using the latest corrected yields (from last iteration) to fit an updated VBS to again use in the next round of compound fate modeling and  $\Phi$  calculations. Ten iterations were always sufficient to achieve convergence (which can be seen graphically in the figures discussed in sections 3.1.1 and S2). VBS fit parameters were constrained to be positive.

**2.5. Modeling RO<sub>2</sub> Fate Regimes.** The KinSim kinetics model<sup>64</sup> was also used to predict the reaction pathways of RO<sub>2</sub> for the regimes discussed above. Because the rate coefficients for these organic nitrate RO2 reactions are not known, estimates are obtained by an examination of available literature on structurally similar RO<sub>2</sub> (Table S6). In the case of the reaction rate for  $RO_2$  +  $RO_2$ , a wide range of values from 2  $\times$  $10^{-17}$  (for tertiary RO<sub>2</sub>) to  $1 \times 10^{-12}$  cm<sup>3</sup> molecule<sup>-1</sup> s<sup>-1</sup> is supportable based on the literature.  $^{35,36}$  A value of 2 × 10<sup>-15</sup> cm<sup>3</sup> molecule<sup>-1</sup> s<sup>-1</sup> is chosen as the best guess for the modeling reported here as the estimate for a tertiary RO2 with a factor of 100 increase in rate due to the beta substituent nitrate group,  $^{35,65}$  and  $1 \times 10^{-12}$  cm<sup>3</sup> molecule<sup>-1</sup> s<sup>-1</sup> as the upper limit.  $^{36}$  We note that in a computational study, Kurtén et al. 66 found that the distributions of tertiary/secondary RO<sub>2</sub> are 65:35 and 60:40 for  $\alpha$ -pinene and  $\Delta$ -carene, respectively. It has been estimated that secondary RO2 generally react ~2 orders of magnitude faster,<sup>35</sup> including a study that compared betahydroxy secondary versus tertiary RO<sub>2</sub>. 67 In part for that reason, we chose the higher range for expected rate increase due to the RO2 beta substitution (estimated as 10- to 100fold<sup>35</sup>). If indeed the Kurten et al.<sup>66</sup> calculations are applicable, then  $2 \times 10^{-15}$  should be considered more of a lower-limit estimation. However, evidence from our own experiments, exploring hydrolysis loss of pRONO<sub>2</sub>, support that the nitrates formed are dominantly not tertiary (section 3.5). Given the uncertainties in the generalized rate estimation assumptions and branching ratios calculations, as well as the additional consideration of cross-reaction rates between different RO2 types, for simplicity we do not choose to use a weighted rate coefficient. In the extreme case, if all RO2 radicals are secondary, then this would give an estimate of  $2 \times 10^{-14} - 2 \times$ 

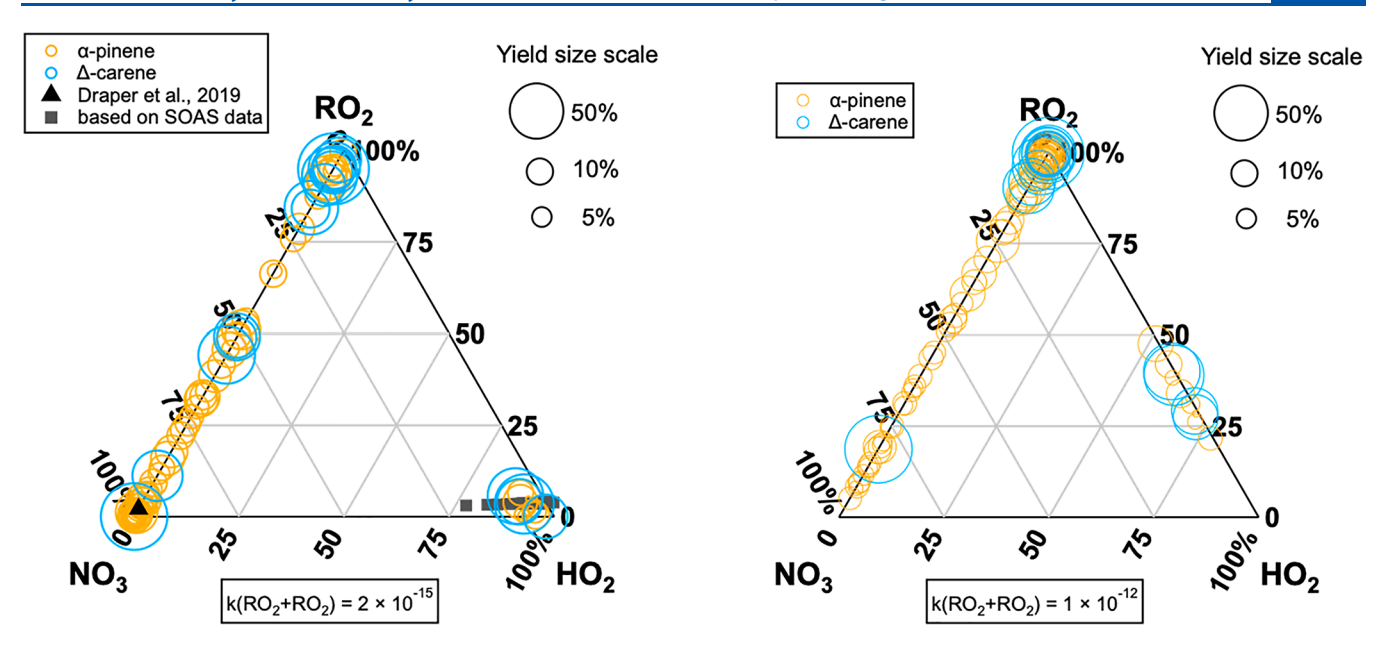


Figure 3. Modeled  $RO_2$  fates displayed in ternary plots, with yields shown for α-pinene (orange) and Δ-carene (blue) with circle size corresponding to yield. Each corner of the triangle represents 100%  $RO_2 + X$ , where X is the species labeled at that point; mixed cases fall along the side with the proportional distance from each point indicating the mix. See text for discussion; these plots demonstrate that SOA yields are not dependent on  $RO_2$  fate for either terpene. We determine the mix of  $RO_2$  bimolecular fate assuming, the following: left: best estimate,  $2 \times 10^{-15}$  cm<sup>3</sup> molec s<sup>-1</sup>, and right: high estimate,  $1 \times 10^{-12}$  cm<sup>3</sup> molec s<sup>-1</sup>, of the  $RO_2 + RO_2$  rate coefficient. Also shown in the left panel are gray square points indicating the  $RO_2$  fate regime for an example in the real atmosphere, based on  $RO_3$  and  $RO_2$  data from the SOAS 2013 campaign, assuming  $RO_2 = 3[HO_2]$ , and a black triangular point showing the  $RO_2$  fate regime in a recent chamber study.

Table 1. Summary of Results from Chamber Experiments<sup>a</sup>

precursor and regime	O/C incl. NO <sub>3</sub> O	O/C std AMS org	H/C	pRONO <sub>2</sub> / SOA	OA (μg m <sup>-3</sup> )	SOA mass yield (%)	VWL corr SOA mass yield (%)
$\alpha$ -pinene RO $_2$ + HO $_2$	$0.46 \pm 0.31$	$0.36 \pm 0.30$	$1.83 \pm 0.08$	$0.12 \pm 0.06$	$8.0 \pm 13$	$3.5 \pm 3.0$	$5.6 \pm 4.6$
$\alpha$ -pinene RO <sub>2</sub> + NO <sub>3</sub>	$0.48 \pm 0.14$	$0.40 \pm 0.13$	$1.78 \pm 0.14$	$0.12 \pm 0.03$	$12.3 \pm 10$	$6.2 \pm 1.3$	$8.9 \pm 4.4$
$\alpha$ -pinene RO <sub>2</sub> + RO <sub>2</sub>	$0.40 \pm 0.10$	$0.30 \pm 0.08$	$1.74 \pm 0.13$	$0.13 \pm 0.03$	$23.1 \pm 20$	$9.9 \pm 4.3$	$12.5 \pm 3.7$
$\Delta$ -carene RO <sub>2</sub> + HO <sub>2</sub>	$0.65 \pm 0.06$	$0.54 \pm 0.05$	$1.79 \pm 0.04$	$0.14 \pm 0.01$	$14.4 \pm 5.5$	$28 \pm 10$	$44 \pm 13$
$\Delta$ -carene RO <sub>2</sub> + NO <sub>3</sub>	$0.56 \pm 0.09$	$0.43 \pm 0.08$	$1.73 \pm 0.04$	$0.16 \pm 0.01$	$11.1 \pm 7.1$	$23 \pm 15$	$41 \pm 20$
$\Delta$ -carene RO <sub>2</sub> + RO <sub>2</sub>	$0.50 \pm 0.06$	$0.40 \pm 0.05$	$1.86 \pm 0.05$	$0.14 \pm 0.02$	$50 \pm 59$	$35 \pm 14$	$43 \pm 18$

"Showing average and standard deviations of chemical composition, total OA, and SOA mass yield (with and without vapor wall loss corrections) for each precursor and each RO<sub>2</sub> regime. For the experiments with sequential additions, OA and SOA mass yield were averaged for each experiment prior to averaging to each regime. Overall estimated relative uncertainty in these SOA mass yields is 30–50%, given the uncertainties in the precursor amount consumed, SMPS volume measurements, wall loss corrections, AMS-derived aerosol composition, and density calculation. These data, as well as more detail on the RO<sub>2</sub> regime for each individual experiment, are shown in Table S1. Table S2 reports the initial conditions for each experiment.

 $10^{-13}$ , still much smaller than the upper limit that we consider. We find it useful to present results for the wider bounds for these possible rate coefficients to show more robustly that experiments were conducted under dominant conditions for all of the main bimolecular  $RO_2$  fates.

We evaluated the sensitivity of the  $RO_2$  fate regime to this rate coefficient, as shown in the ternary plots of Figure 3. For batch experiments, the box model was initialized using observed initial concentrations of VOC,  $N_2O_5$ ,  $NO_3$ ,  $NO_2$ ,  $O_3$ , and  $H_2O$ , and the regime was determined by assessing the cumulative amount of  $RO_2$  reacted by each pathway at the time of yield determination, as a percentage of total  $RO_2$  reacted. For all  $RO_2 + HO_2$  experiments, and several multistep experiments,  $N_2O_5$  was continuously added to the chamber. For these experiments, a continuous injection of  $N_2O_5$  was included in the model, in addition to discrete injections of HCHO and VOC.  $N_2O_5$  and  $NO_3$  gas-phase wall losses were

included in the model, based on experimental determination (Figure S12).

In the model, first-generation products of  $RO_2 + RO_2$ ,  $RO_2 + HO_2$ , and  $RO_2 + NO_3$  reactions were tracked in order to determine the fraction of the  $NO_3$ -produced  $RO_2$  that went via each reaction pathway, assuming these are the sum total of the possible  $RO_2$  fates. These are reported in Table S1 for our best estimate of the  $RO_2 + RO_2$  rate coefficient ( $2 \times 10^{-15}$  cm<sup>3</sup> molec s<sup>-1</sup>). An additional reaction pathway for the  $RO_2$  radical is to produce metastable peroxyalkyl nitrates (PNs) via  $RO_2 + NO_2$  reactions. These experiments spanned a range of  $NO_2$  concentrations from <10 to 500 ppb. The effect of  $RO_2 + NO_2$  chemistry is to temporarily sequester some portion of the  $RO_2$ . Thermal dissociation will re-release these  $RO_2$  and  $RO_2$  on the seconds time scale, so this reservoir does not substantially affect the  $RO_2$  fate regimes under most conditions; the kinetic modeling included these  $ROONO_2$  production and dissocia-

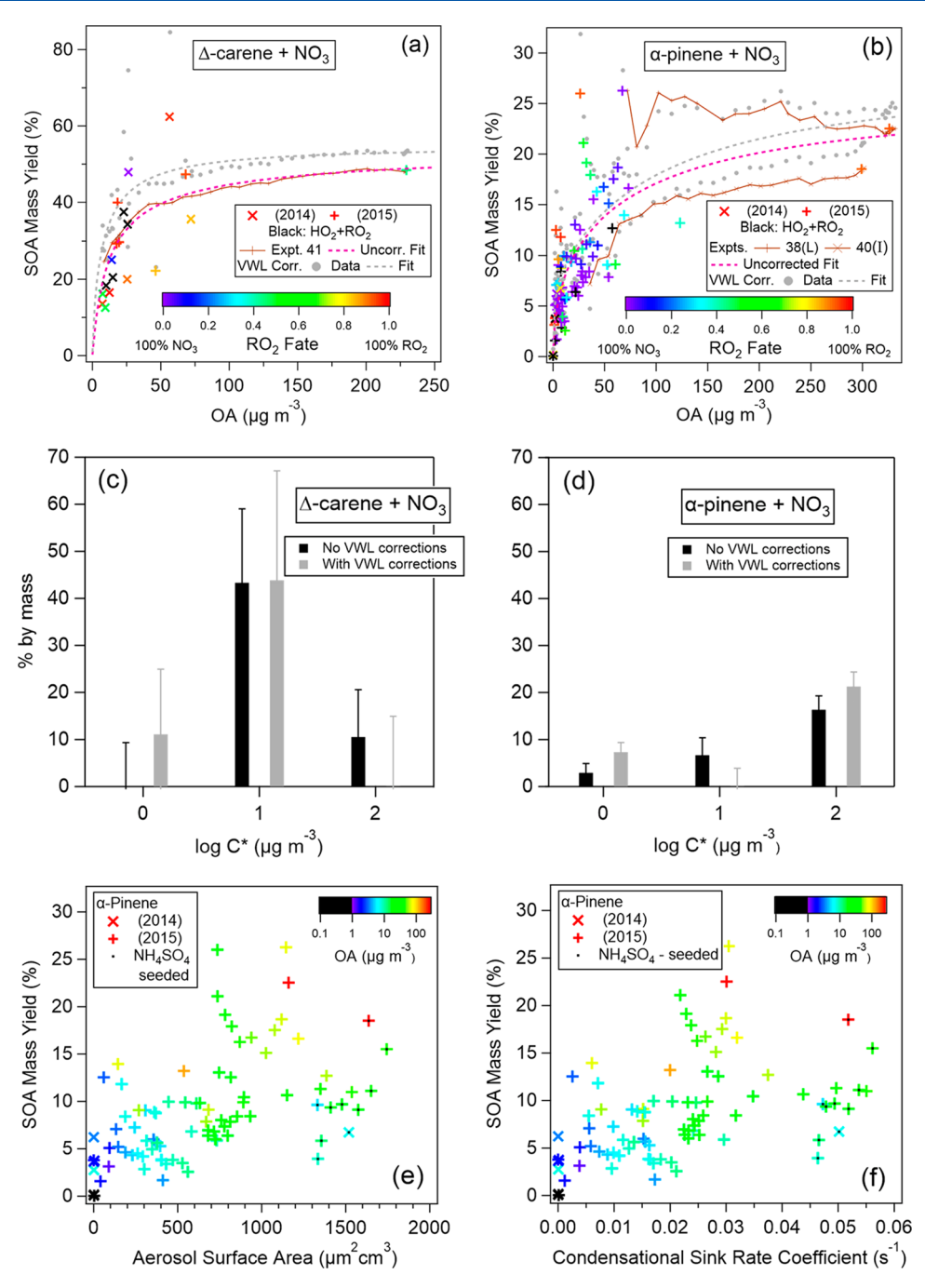


Figure 4. SOA mass yield vs OA concentration for (a)  $\Delta$ -carene + NO<sub>3</sub> and (b)  $\alpha$ -pinene + NO<sub>3</sub>. Yield curves are shown without (colored points/black, color coded by RO<sub>2</sub> fate as indicated) and with (gray) vapor-phase wall loss (VWL) correction (Case 3) applied; see discussion in section 3.1.1. In addition to final yield results from each individual reaction step (per Tables S1 and S2), intermediate data are included from a few experiments where reaction was gradual and spanned a large range of OA, to better constrain the yield curves at higher OA (brown markers/lines). SOA mass yield increases as a function of OA regardless of modeled RO<sub>2</sub> fate, with no systematic differences among regimes. (This is also true of the VWL-corrected data.) RO<sub>2</sub> fates are modeled for the case of RO<sub>2</sub> + RO<sub>2</sub> rate coefficient of 2 × 10<sup>-15</sup>; all experiments indicated as "HO<sub>2</sub> + RO<sub>2</sub>" were modeled as 88% or higher HO<sub>2</sub> fate. Panels (c) and (d) show the volatility basis sets derived from fitting the yield curves, with error bars representing the fit uncertainty of the uncorrected and final Φ-corrected yields. Panels (e) and (f) show SOA yield vs aerosol surface area and vs aerosol condensational sink, for α-pinene + NO<sub>3</sub> (for all RO<sub>2</sub> fate regimes and with organic and inorganic seed particles). This shows that when seeding the chamber with inorganic seeds with large surface area (points that lie to the lower right of the plot, marked with black squares), the yields are not strongly influenced by the additional surface area alone but rather depend on final OA loading (coloring). This supports that the increasing yields for all experiments are primarily driven by available OA mass (absorptive partitioning) rather than aerosol surface area (offsetting kinetics of wall-effects). All yields and OA concentrations have been corrected for particle-wall losses. Aerosol surface areas and condensational sink rate coefficients shown are from the period immediately prior to initiating the α-pinene + NO<sub>3</sub> reaction. The values for th

tion reactions and thus it has been taken into account. The modeled relative RO<sub>2</sub> reactive fates were used to construct the ternary plots shown in Figure 3.

We note that the ternary plots in Figure 3 ignore the possibility of a unimolecular autoxidation pathway. Calculated rate coefficients for atmospheric RO2 H-shift reactions range from  $8 \times 10^{-4} \,\mathrm{s}^{-1}$  (Crounse et al., <sup>68</sup> for a generic unsubstituted 1,5 H-shift) to as fast as 1 s<sup>-1</sup> (Knap et al.,<sup>69</sup> for a 1,5 H-shift in 3-methyl-3-buten-1-ol). Kurtén et al. 66 showed that for all conformers of the initially formed  $\alpha$ -pinene and  $\Delta$ -carene nitrato-peroxy radical, H-shift reaction rate coefficients are below  $10^{-4}$  s<sup>-1</sup>, ruling them out as a major pathway. More recently, Draper et al. 65 calculated RO<sub>2</sub> H-shift rate coefficients for various conformers of the subsequently formed RO2 radicals and found the fastest possible H-shift rate in the  $\Delta$ carene system to be  $8.0 \times 10^{-2} \text{ s}^{-1}$ , concluding that under atmospheric conditions, only select RO<sub>2</sub> H-shift reactions would be competitive with bimolecular RO2 + RO2 and RO<sub>2</sub>+HO<sub>2</sub> reactions. However, both papers posited that latergeneration RO2, formed after an alkoxy radical mediated ringopening step, could autoxidize faster.

#### 3. RESULTS AND DISCUSSION

A summary of yields for each regime is shown in Table 1. The ternary yield plots (Figure 3) illustrate both how well the experiments conducted spanned the range of potential RO2 fates (RO<sub>2</sub> + RO<sub>2</sub>, RO<sub>2</sub> + NO<sub>3</sub>, and RO<sub>2</sub> + HO<sub>2</sub>), as well as showing that there was no significant difference in SOA yield across the RO<sub>2</sub> fates for each precursor,  $\alpha$ -pinene (orange) and  $\Delta$ -carene (blue). We see that assuming no autoxidation, unless the  $RO_2 + RO_2$  reaction rate is very low (this is unlikely; see Berndt et al. 42), then we successfully spanned the range of RO<sub>2</sub> bimolecular fates. Δ-Carene SOA yield was uniformly high, while  $\alpha$ -pinene yield was uniformly low. The major finding of this study is that SOA yield for  $\Delta$ -carene is always substantially larger than SOA yield for  $\alpha$ -pinene, regardless of the relative concentrations of RO2, HO2, and NO3, which should dictate RO<sub>2</sub> bimolecular fate. Below, we further detail the observations of SOA yield from both precursors, then we explore potential explanations for this similarity across reaction conditions and stark difference between VOC precursors. Bulk chemical compositions of the systems are also explored, as well as dependencies of yields on OA concentrations, including derivation of volatility basis sets applicable to atmospheric modeling.

**3.1. SOA Mass Yields across RO<sub>2</sub> Fate Regimes.** Table 1 and Figure 3 above present SOA mass yields from all experiments, showing that this set of experiments most likely spanned the parameter spaces of  $RO_2$ ,  $HO_2$ , and  $NO_3$  dominated reactions. The two panels illustrate the problem that arises from the large range of literature  $RO_2 + RO_2$  rate coefficients: Without better knowledge of this rate coefficient in the case of these experiments, where the initial  $RO_2$  produced will be predominantly  $\beta$ -nitrato substituted tertiary  $C_{10}$  peroxy radicals, we cannot be certain that  $RO_2 + HO_2$  dominated conditions were achieved.

For reference, Figure 3 also shows modeled RO<sub>2</sub> fate regime results using nighttime data from the SOAS campaign. HO<sub>2</sub> was measured by the Ground-based Tropospheric Hydrogen Oxides Sensor (GTHOS), and the steady-state NO<sub>3</sub> concentration is from calculations in Ayres et al. The concentration of RO<sub>2</sub> is assumed to be triple that of HO<sub>2</sub>. Given these estimates of RO<sub>2</sub>, HO<sub>2</sub>, and NO<sub>3</sub> concentrations,

we find that  $HO_2 + RO_2$  dominates over  $RO_2$  or  $NO_3$  in terms of the bimolecular fate of the initially formed  $RO_2$ . The apparent relative unimportance of  $RO_2$  reaction with  $NO_3$  for the SOAS example can be framed in context of the short  $NO_3$  lifetime (and thus low concentrations) for biogenic-rich conditions during nighttime due to rapid reaction of  $NO_3$  with olefinic VOC: The reaction of  $NO_3$  with VOC simply outcompetes the reaction of  $NO_3$  with  $RO_2$ . Thus, in such environments, the importance of  $NO_3$  for oxidation of compounds with one double bond may be limited to the initial  $NO_3$  reaction. More precise assessment of the relative importance of reaction with  $RO_2$  versus  $HO_2$  requires more detailed mechanistic information and better constraints on the relevant  $RO_2 + RO_2$  rates.

Several organic seeded experiments enabled us to explore the SOA yield as a function of organic aerosol mass loading, across RO2 fate regimes and for both precursors. These results are plotted in Figure 4, with volatility basis set (VBS) fits to the yield curves for  $\alpha$ -pinene and  $\Delta$ -carene, both with and without corrections for vapor-phase losses to chamber walls (see section 3.1.1 below). We note that  $\Delta$ -carene yields are substantially larger than  $\alpha$ -pinene, and with both precursors, yield measurements track along the same curve as a function of organic aerosol (OA) concentration, regardless of RO<sub>2</sub> fate regime. This independence of yield as a function of RO2 fate regime persists after correcting for VWL, shown in Figure S13. This is consistent with a similar study reported in Boyd et al.<sup>39</sup> for NO<sub>3</sub> +  $\beta$ -pinene, which show an aerosol mass yield curve closer to the larger yields found here for  $\Delta$ -carene (60% at organic mass loading of 40  $\mu g$  m<sup>-3</sup>) and likewise independent of RO<sub>2</sub> fate regime (those authors tested RO<sub>2</sub> + NO<sub>3</sub> and RO<sub>2</sub> + HO<sub>2</sub> regimes). Devault and Ziemann<sup>73</sup> reported a mass yield of 56  $\pm$  2% for SOA formed from NO<sub>3</sub> +  $\Delta$ -carene under an  $RO_2 + RO_2$  fate regime at hundreds of  $\mu g \text{ m}^{-3}$  OA, very comparable to our observations that appear to approximately plateau at ~50% at high OA. In contrast, Devault et al. 45 observed a mass yield for NO<sub>3</sub> +  $\alpha$ -pinene of 48% (for similar reaction conditions to Devault and Ziemann), <sup>73</sup> which is substantially higher than our yields of 20–25% for NO<sub>3</sub> +  $\alpha$ pinene at higher OA.

3.1.1. Compound Fate Modeling of Vapor-Phase Wall Losses and Yield Correction Factors. The compound fate modeling, yields corrections, and VBS estimation outlined in section 2.4 were conducted for different cases, using different assumptions about the presence, treatment, and effects of preexisting SOA (hereafter, "pxSOA") in the chamber at the beginning of a given reaction step. This primarily affects experiments where OA increases during a multistep reaction sequence, and experiments where injection of N2O5 prior to the experiment produced small amounts of background OA. Table S5 summarizes the different cases used in modeling subsequent semivolatile partitioning and wall losses. "Case 0" is the base case, in which any pxOA is treated as nonvolatile (but still available for absorptive partitioning as part of the total OA). Here "pxOA" is used to refer to any OA present in the chamber prior to each planned NO<sub>3</sub> + terpene reaction, whether SOA or not (so may be OA seed or SOA from previous planned or unintended chemistry). The distinction between pxSOA and pxOA can be important in some cases since some components of OA (such as DOS added as seed) should always be treated as nonvolatile, whereas SOA produced from chemistry can be treated as semivolatile, with different volatility and equilibria assumptions as done here.

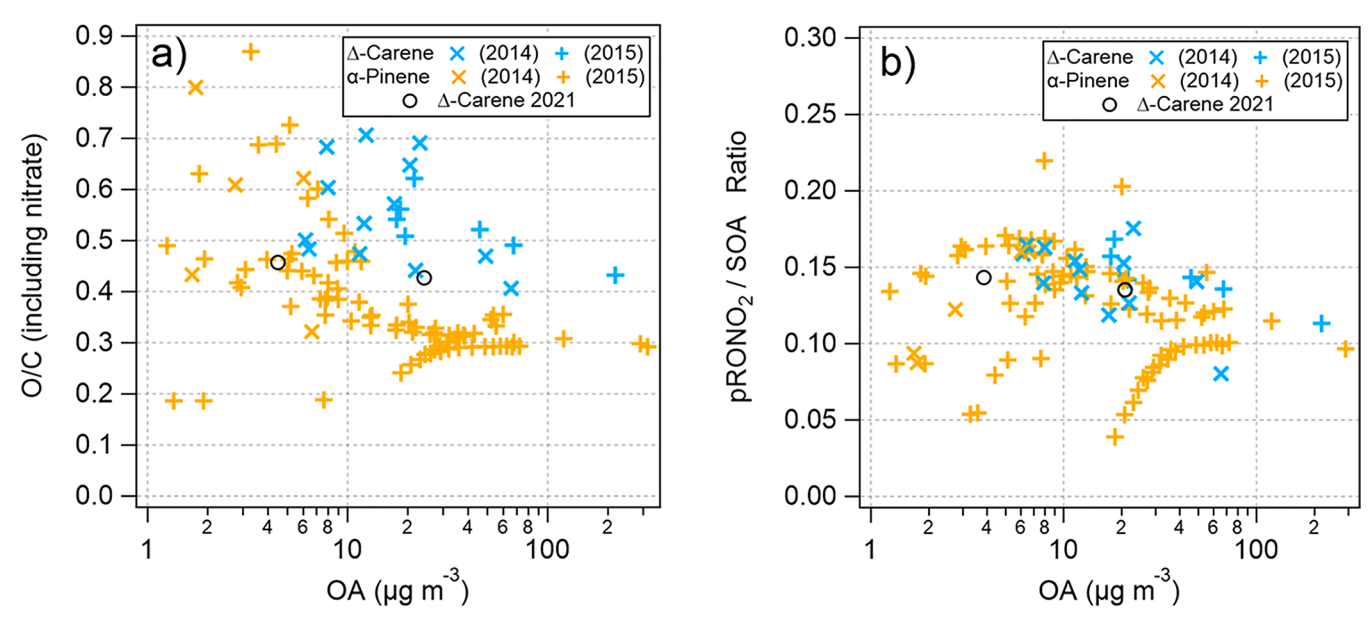


Figure 5. O/C (a) and pRONO<sub>2</sub>/SOA (b) ratios vs OA. O/C ratios include all of the oxygen contribution from pRONO<sub>2</sub>. See Figure S7 for equivalent O/C plots for excluding additional oxygen from nitrate (per "standard AMS organics" elemental ratios). Figures S7 and S9 show comparisons of these plots to those using different RIE<sub>SOA</sub> and collection efficiency assumptions.

The other four cases considered pxSOA as initially in equilibrium only with gas-phase (Case 1), in equilibrium with gas and chamber wall phases (Case 2), in equilibrium with gasphase and with only higher-volatility compounds in equilibrium with the walls (Case 3), and a variation on Case 3 where pxSOA was only considered for experiments where prior oxidation steps were conducted (Case 4). Section S2 describes and compares the results for each of the different treatments in context of  $\Phi$ 's (and their dependencies), yields curves, and VBS. Figures S14-S18 provide summaries of each case separately, and Figures S19 and S20 directly compare  $\Phi$ 's, yield curves, and VBS among the cases. Overall, the computed yield curves and VBS did not show large differences; however, small shifts in magnitude and shapes were observed. All cases showed substantial increases in yields at some or all of the OA range compared to that without any VWL considerations. We take Case 3 to be the most realistic treatment to reconstruct wall-free yields, due to its most realistic treatment of pxSOA. Therefore, Case 3 is shown in Figure 4, as the recommended corrected yield curve and VBS. The derived yield correction factors for most experiments are modest ( $\Phi = 0.9-1.7$ , Figure S17a,b) but for some experiments (primarily  $\alpha$ -pinene at low loading) can range up to 2-5.

The Supporting Information contains more details on modeling evaporation as an alternative approach to constraining the lower volatility  $C^*$  bins for  $\Delta$ -carene (section S3). Evaporation modeling of  $\Delta$ -carene SOA was conducted due to the limited yield data at lower OA concentrations and thus lack of strong constraints of the VBS at lower volatility, as well as the availability of experiments where the SOA was held in the reaction chamber for hours after oxidation, unperturbed. A hybrid (and iterative) approach was used to constrain the lower volatility bin ratios using the evaporation profile from four extended experiments and then all experiments for the yield curve fitting. This method produced similar yield curves and VBS, on average; however, given the interexperiment variability among the evaporation fitting results, we conclude that substantially stronger constraints for the  $\Delta$ -carene SOA

VBS were not determined in this case. Nevertheless, the approach is a potential additional method for constraining VBS by a combination of yields and evaporation. Applying this approach to a larger set of experiments, with greater variability in initial OA concentrations, could provide stronger constraints.

**3.2.** Average Aerosol Composition by AMS and FG Analysis. Throughout the experiments, we observed strikingly similar aerosol composition (as characterized by the AMS), as shown in the representative spectra from  $\Delta$ -carene + NO $_3$  in each RO $_2$  regime (Figure S23), and to a slightly lesser degree in the representative spectra from  $\alpha$ -pinene + NO $_3$  in each RO $_2$  regime (Figure S24). Table S7 reports the uncentered correlation coefficients (UC) pairwise among mass spectra from the various RO $_2$  regimes and for the two precursors. This analysis demonstrates that within each VOC precursor the similarity across RO $_2$  regimes (UCs 0.89–0.98) is generally greater than the similarity across the two precursors for the same RO $_2$  regime (UCs 0.78–0.92).

The yield table above (Table 1) also reports AMS measured particle-phase organic nitrate contribution to SOA (pRONO<sub>2</sub>/SOA) and SOA elemental ratios, which demonstrates that the consistency of SOA mass yields for both  $\Delta$ -carene and  $\alpha$ -pinene in the various RO<sub>2</sub> fate regimes coincides with a striking similarity in pRONO<sub>2</sub> fraction; regardless of the most likely bimolecular reaction partner, the aerosol formed has on average 0.12–0.16 pRONO<sub>2</sub>/SOA.

3.2.1.  $\Delta$ -Carene +  $NO_3$  SOA. In order to assess the types of molecules that constitute the SOA formed in the  $\Delta$ -carene reactions, we combined the observations of bulk pRONO<sub>2</sub>/SOA, O/C, and H/C for data at OA  $\sim 10~\mu g$  m<sup>-3</sup>. For that, we use a pRONO<sub>2</sub>/SOA mass ratio of 0.15, and O/C and H/C molar ratios of the organic fraction of 0.45 (excluding additional O from nitrate) and 1.8 (see Figure S7 for O/C, Figure Sb for pRONO<sub>2</sub>/SOA, and Table 1 for H/C). This yields an average molecular formula of the condensing material of  $C_{10}O_{3.9}H_{18}(NO_3)_{0.57}$  for monomeric  $C_{10}$  units. Thus, approximately three-fifths of every  $C_{10}$  unit in SOA is

estimated to contain a nitrate functional group. The remaining oxygens (~4 per C<sub>10</sub> unit) would be consistent with one OH or C=O functionality per ~2.5 carbon atoms, or one OOH per 5 carbon atoms. We note that dimers need not be the dominant condensing species. However, if C<sub>20</sub> molecules were the major species constituting the aerosol, then they would carry approximately 8 non-nitrate oxygens per C20 unit, and they would have on average 1.14 nitrate functional groups. Note that in the above estimate of the bulk average molecular formula, it is assumed that one of the oxygens from each nitrate functional group is measured as part of the AMSmeasured organic signal, in accordance with previous observations.<sup>74</sup> Section S1.1.3 and Table S3 show the composition inputs and computed estimates of average molecular formulas for the upper/lower reasonable ranges of pure SOA collection efficiency (and associated RIE<sub>SOA</sub>), which are  $C_{10}O_{4.0}H_{18}(NO_3)_{0.49}$  and  $C_{10}O_{3.8}H_{18}(NO_3)_{0.68}$ .

For comparison, Devault and Ziemann<sup>73</sup> reported an average O/C value of 0.45  $\pm$  0.07 for functional group analysis of SOA formed from  $NO_3 + \Delta$ -carene ( $RO_2 + RO_2$ dominated, at several hundred  $\mu g$  m<sup>-3</sup> SOA), which is very similar to the O/C values (including nitrate oxygen) observed here at the higher OA concentrations (0.4-0.5; Figure 5a). Their reported H/C was  $1.71 \pm 0.09$ , which is similar, but slightly lower than the 1.8-1.9 observed here at higher OA concentrations. In contrast, they observed substantially higher pRONO<sub>2</sub>/SOA ratios of 0.26 by mass or 0.94  $\pm$  0.1 nitrate groups per C<sub>10</sub>, even comparing to our higher estimate for the lower CE limit (0.68 nitrate per  $C_{10}$ ). While the mechanisms presented in Devault and Ziemann<sup>73</sup> support only minor pathways for formation of molecules without nitrate, it is not clear why the two methods yield substantially different nitrate contributions. The method used here may have substantial uncertainties due to the fact that it relies on the quantitative comparison of AMS mass and SMPS volume concentrations measurements in order to constrain the RIE of the SOA. Considering only the uncertainty associated with the base sensitivity calibration of the AMS (ammonium nitrate sensitivity calibration), since RIE and CE are constrained separately, gives an uncertainty of of that comparison of  $\pm 10\%$ for AMS and ±30% for SMPS volume, 75 so a combined uncertainty of  $\pm 32\%$ . That, combined with the reported uncertainty in the DeVault and Ziemann functional group analysis, could account for most of the discrepancy for the best estimate CE (CE = 0.875; 0.57 nitrate per  $C_{10}$ ) or all for the lower CE range (CE = 0.75; 0.68 nitrate per  $C_{10}$ ).

A possible bias could also be related to the applied RIE for pRONO<sub>2</sub> (assumed to be equal to that measured for ammonium nitrate here). While several laboratory and field comparisons of AMS pRONO<sub>2</sub> quantification versus independent quantification methods (including one using data from this study) do not support a systematically different RIE for pRONO<sub>2</sub>, <sup>57</sup> one report for a few isolated organic nitrates from oxidation of monoterpenes and isoprene generated in the laboratory, suggest it may be a factor of 2 lower for those compounds. 76 Applying an RIE of pRONO<sub>2</sub> of a factor of 2 lower to this analysis would increase the nitrate contributions to 0.98-1.36 nitrate group per  $C_{10}$ . However, further studies would be required to broadly support this treatment. Finally, we note that simply applying the default RIE to the AMSmeasured standard organic component (1.4) rather than that estimated here (2.36), as has typically been done for laboratory studies, would lead to much lower estimates of nitrate contributions to SOA.

3.2.2.  $\alpha$ -Pinene + NO<sub>3</sub> SOA. For  $\alpha$ -pinene, as noted above, a clear dependence of SOA yields on OA concentration has been found (Figure 4). This result suggests that the primary products from the  $\alpha$ -pinene + NO<sub>3</sub> reactions are semivolatile. Furthermore, we observe a shift in aerosol composition to greater oxidation as a function of OA loading: in an experiment in which OA progressively increased (experiment 37; Figures 2 and S25), the early formed SOA at low loading (1.3  $\mu$ g m<sup>-3</sup>) has O/C ratio of 0.49, while later, at higher loading (28  $\mu$ g  $m^{-3}$ ), the O/C ratio decreases to 0.32, suggesting that the initial SOA formation is enabled by highly oxidized species present in smaller concentrations, upon which less oxidized species can subsequently condense. Overall, the O/C ratio is clearly anticorrelated with OA loading for  $\alpha$ -pinene + NO<sub>3</sub> SOA; in the case of  $\Delta$ -carene + NO<sub>3</sub> SOA, this dependence is less apparent (Figure 5a). A similar dependence was observed in  $\alpha$ -pinene + O<sub>3</sub> SOA.<sup>77</sup> Similarly to  $\Delta$ -carene, the bulk average molecular formula can be estimated from the observations, in this case using pRONO<sub>2</sub>/SOA of 0.155, O/ C of 0.30 (excluding additional O from nitrate), and H/C of 1.8 (again for average values at OA  $\sim 10 \,\mu \mathrm{g \ m^{-3}}$ ). This yields a formula of  $C_{10}O_{2.5}H_{18}(NO_3)_{0.50}$ , a slightly lower nitrate group contribution, and ~1.5 fewer non-nitrate oxygens per C<sub>10</sub> monomer, compared to  $\Delta$ -carene. The lower contribution of functional groups is generally consistent with the lower yields and higher volatility character, although the identity of those functional groups and the degree of oligomerization may also be a factor. Additionally, given the substantial trend in O/C with OA concentration (and to a lesser degree in pRONO<sub>2</sub>/ SOA), for lower OA concentrations, the amount of non-nitrate oxygen and nitrate groups in the condensing molecules will be larger, which may be particularly relevant for relatively unpolluted regions with substantial  $\alpha$ -pinene + NO<sub>3</sub> chemistry. Section S1.1.3 and Table S3 show the composition inputs and computed estimates of average molecular formulas for the upper/lower reasonable ranges of pure SOA collection efficiency (and associated RIESOA), which are  $C_{10}O_{2.6}H_{18}(NO_3)_{0.42}$  and  $C_{10}O_{2.4}H_{18}(NO_3)_{0.57}$ .

We compare again to estimates of O/C and pRONO<sub>2</sub>/SOA from functional group analysis for the products of NO<sub>3</sub> +  $\alpha$ -pinene, conducted at higher OA concentrations. DeVault et al. reported an average O/C ratio of 0.32  $\pm$  0.05 for functional group analysis of SOA formed from NO<sub>3</sub>+ $\alpha$ -pinene (RO<sub>2</sub> + RO<sub>2</sub> dominated, at ~200  $\mu$ g m<sup>-3</sup> ammonium sulfate seed), which is very similar to the asymptote ratio found here at larger OA (0.30; Figure 5a). The degree of nitrate functionalization found in that study, like that from NO<sub>3</sub> +  $\Delta$ -carene, is substantially higher, with 0.94  $\pm$  0.28 nitrate functional groups per C<sub>10</sub> molecule, which corresponds to a pRONO<sub>2</sub>/SOA ratio of 0.29, in contrast to the 0.10–0.13 observed here for larger OA (Figure 5b).

3.2.3. Peroxide Contribution Quantified by Functional Group (FG) Analysis. In order to better compare the experimental conditions used in this study to the functional group (FG) analyses previously carried out by colleagues in the Ziemann group,  $^{45,73}$  with particular focus on the production of organic peroxides, we repeated one of our experiments to collect filtered SOA mass for FG analysis. The experiment began with 11 ppb  $N_2O_5$  and 100 ppb  $\Delta$ -carene to mimic our typical  $RO_2 + RO_2$  regime conditions. This produced only 4  $\mu$ g m<sup>-3</sup>, so a second injection of 11 ppb  $N_2O_5$  was added to

produce enough mass for filter FG analysis (23  $\mu$ g m<sup>-3</sup>). Subsequently, SOA was collected on a filter for 150 min, during which time the SOA loading in the chamber decreased to 15  $\mu$ g m<sup>-3</sup>. We note that the weighted mass of aerosol on the filter was 2.0 times higher than predicted by the SMPS, for 1.27 g cm<sup>-3</sup> density. Subsequent tests with DOS aerosol added to the chamber and similarly measured with the SMPS and filter collection, confirmed that this total mass uncertainty is approximately 25%. Therefore, for the calculation of FG contributions to total SOA, we use the filter mass weighing for total mass of SOA collected (not SMPS). This follows from the assumption that the additional mass collected on the filter may have been semivolatile vapors of similar composition to bulk SOA. Otherwise, computing SOA mass using the SMPS would approximately double the peroxide functional group contributions discussed below. The O/C and pRONO<sub>2</sub>/SOA ratios for this experiment are indicated in Figure 5 for both reaction steps which were similar to other  $\Delta$ -carene experiments (albeit with O/C values at the lower end of the observed range).

The functional group analysis yielded  $5.9 \times 10^{-4}$  moles of peroxide per gram SOA. This equates to on average 14% of C<sub>10</sub> monomers containing a peroxide functional group and 7.1% of the non-nitrate oxygen coming from peroxides (for molecular weight of 237 g mol<sup>-1</sup> and 3.9 non-nitrate oxygen per C<sub>10</sub>; see Table S3). This ratio is consistent with DeVault and Ziemann<sup>73</sup> and supports the conclusion that autoxidation is not a major route to forming condensable material in these experiments, since that would be expected to produce substantial numbers of (hydrogen) peroxide functional groups per C<sub>10</sub>. It also supports that ROOR formation (in the gas or particle phase) is not a major pathway for bulk SOA formation. We acknowledge that we only conducted this functional group analysis for the RO<sub>2</sub> + RO<sub>2</sub> regime, but given the composition similarities, it is reasonable to expect that the NO<sub>3</sub> and HO<sub>2</sub> regimes follow a similar pathway. Additional evidence supporting the unlikely importance of autoxidation is presented in section 3.3 below. Thus, if neither autoxidation nor ROOR formation can explain the higher SOA yields for  $NO_3 + \Delta$ -carene, then the likely explanation is the production of similar alkoxy radical, which can then isomerize to add oxygens (predominantly forming ketone/aldehyde/alcohol functional groups) until these monomers are low enough volatility to condense. Further context from the literature as well as additional evidence from this study in support of this conclusion are presented in the following section.

3.3. Interpretation of Similar SOA Mass Yields from  $RO_2 + NO_3/RO_2/HO_2$  Chemistry. The observation of very similar yields across different RO<sub>2</sub> bimolecular fates is striking. Relatively few chamber experiments have been conducted exploring the RO<sub>2</sub> fate regime dependence of SOA yields from NO<sub>3</sub> initiated SOA production; in fact, review papers have urged that more studies of the effect of competing RO2 reaction pathways on SOA yield are needed to improve model mechanisms. 18,78 Ng et al. 79 found that SOA produced in the isoprene +  $NO_3$  system came primarily from  $RO_2$  +  $RO_2$ reactions, with lower SOA yield observed when reaction conditions were dominated by RO<sub>2</sub> + NO<sub>3</sub>. Another study on SOA formation from isoprene photooxidation similarly found a dependence of SOA volatility on RO2 fate, driven by NOx level.<sup>80</sup> In contrast, SOA produced from  $\beta$ -pinene + NO<sub>3</sub> was observed to be comparable in the  $RO_2 + NO_3$  and  $RO_2 + HO_2$ regimes.<sup>39</sup> However, SOA formed from an approximately equal

mix of  $RO_2 + NO_3$  and  $RO_2 + HO_2$  in  $\alpha$ -pinene +  $NO_3$  vs  $\beta$ -pinene +  $NO_3$  was observed to have markedly different volatility across the BVOC precursors, with  $\alpha$ -pinene SOA evaporating much more readily.<sup>29</sup>

The comparable SOA yields observed in this study across the  $RO_2$  fates in the  $\Delta$ -carene +  $NO_3$  and  $\alpha$ -pinene +  $NO_3$  systems suggest that the condensing species in each regime may be similar in terms of volatility and possibly chemical composition. In the case of  $\Delta$ -carene, which always produces substantial SOA (even in the absence of any seed), similar low volatility products may form across the regimes through the formation and subsequent reactions of alkoxy radicals (RO) or through unimolecular  $RO_2$  loss processes, such as isomerization and autoxidation. In  $\alpha$ -pinene +  $NO_3$ , less highly oxidized species are formed, resulting in substantially less SOA formation, suggesting that these  $RO_2$  follow a different reaction path to more volatile products.

Figure 1 shows that in each regime, the  $RO_2$  radical may react to become an alkoxy radical (R1). The  $RO_2 + NO_3$  reaction has been extensively studied, and RO has been identified as the dominant product:<sup>34,35</sup>

$$RO_2 + NO_3 \rightarrow RO + NO_2 + O_2 \tag{R1}$$

Alternatively, and particularly under high-VOC conditions, RO<sub>2</sub> can react with another RO<sub>2</sub>, with three main reaction pathways possible:

$$RO_2 + RO_2 \rightarrow RO + RO + O_2$$
 (R2a)

$$\rightarrow$$
 ROH + R=O + O<sub>2</sub> (R2b)

$$\rightarrow$$
 ROOR + O<sub>2</sub> (R2c)

The "radical channel" (reaction R2a) in the  $RO_2 + RO_2$  reaction has been found to be the dominant pathway when the carbon attached to the peroxy radical is highly substituted or is oxidized, while the alcohol/carbonyl formation pathway (reaction R2b) has generally been found to be more prominent with small unsubstituted molecules, such as methyl peroxy and ethyl peroxy radicals.  $^{34,81-83}$ 

The organic peroxide (ROOR) channel (reaction R2c) has been measured to be minimal with small molecules, and Kwan et al.<sup>84</sup> quantified the ROOR channel to be small (3-4%) in the RO<sub>2</sub> + RO<sub>2</sub> reaction in isoprene + NO<sub>3</sub>. However, other studies point to a significant role for ROOR in SOA formation in NO<sub>3</sub>-initiated as well as other oxidation systems. Ng et al. 15 suggest that ROOR could be a major SOA component in the isoprene + NO<sub>3</sub> system, finding that peroxides (ROOH + ROOR) were responsible for 17-32% of the SOA mass using mass spectrometry and iodometric spectroscopic methods. Boyd et al.<sup>39</sup> observe ROOR and ROOH products by HPLC-UV-vis at 235 nm in the  $\beta$ -pinene + NO $_3$  system. Claflin and Ziemann<sup>43</sup> also investigated SOA formation from  $\beta$ -pinene + NO<sub>3</sub> and found a 30% yield of highly oxidized oligomeric products in a system where gas-phase chemistry was dominated by RO<sub>2</sub> + RO<sub>2</sub>; however they interpret the oligomeric products not as arising directly from gas-phase  $RO_2 + RO_2 \rightarrow ROOR$  reactions, but rather from later particlephase condensation reactions of the ring-opened  $\beta$ -nitrooxyalkoxy radicals formed in reaction reaction R2a. DeVault et al. 45,73 reported similar results for  $\Delta$ -carene,  $\alpha$ -pinene, and limonene + NO<sub>3</sub> conducted with similar conditions and methods. Berndt et al. 42 recently highlighted more efficient

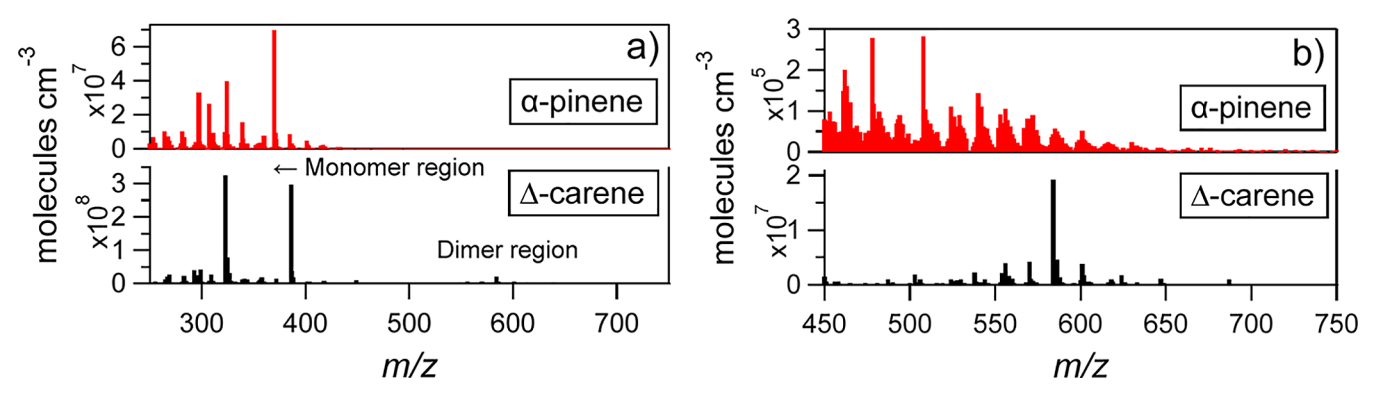


Figure 6. NO<sub>3</sub>–CIMS spectra of gas-phase HOM species detected for both monoterpenes (with monomer and dimer region shown in panel a and highlighting only dimer region in panel b). There are different highly oxygenated molecules (HOM) in the gas phase between α-pinene and  $\Delta$ -carene, and  $\Delta$ -carene has a larger proportion of compounds detected in the dimer range. Spectra shown are for the ions detected, thus most include the NO<sub>3</sub><sup>-</sup> reagent ion. The spectra are from experiments 26 (α-pinene) and 24 ( $\Delta$ -carene). Note the concentration scales for the two terpenes have different scales for both panel pairs; however, the relative values do not directly correspond to the relative amount of HOMs produced for each terpene. This is because different concentrations of terpenes were reacted and the amount of HOMs observed in the gas phase depends on the particle condensational sink and OA available for gas-particle partitioning, which requires modeling to properly account for these factors (see section 3.4 below).

ROOR production from RO2 self-reaction than previous studies (in OH oxidation of 1,3,5-trimethylbenzene). Bell et al. 85 reported that observed aerosol signals were dominated by dimer nitrates for SOA formed from  $\alpha$ -pinene + NO<sub>3</sub> oxidation under RO<sub>2</sub> + RO<sub>2</sub> and RO<sub>2</sub> + NO<sub>3</sub> dominated conditions. Bates et al. <sup>31</sup> reported higher SOA yields for  $\alpha$ -pinene + NO<sub>3</sub> oxidation for experiments estimated to have higher proportion of RO<sub>2</sub> + RO<sub>2</sub> fates, attributed primarily to a high inferred dimer branching ratio (~16%). However, DeVault et al.<sup>45</sup> measured peroxide functional group concentrations in  $\alpha$ pinene + NO<sub>3</sub> SOA to be ~0.01 groups per C<sub>10</sub>, showing that ROOR gas-phase dimer formation does not make significant contributions to SOA for this system. Thus, it is likely that the  $C_{17}$ - $C_{20}$  compounds observed in the SOA filters samples by Bates et al.<sup>31</sup> were formed not from gas-phase dimer formation, but rather particle-phase reactions forming acetal dimers, as has been observed by the Ziemann group to comprise large fractions of SOA for monoterpene + NO3 systems, using techniques with molecular specificity.

The high VOC and oxidant concentrations (ppm levels) used by Kwan et al.,84 Claflin and Ziemann,43 DeVault and Ziemann, 73 and DeVault et al. 45 make it difficult to draw direct comparisons to this set of experiments. However, Ng et al.<sup>79</sup> used lower concentrations (~200 ppb) of VOC and found peroxides in isoprene SOA, which suggests that the small amount of low volatility ROOR products formed in the RO<sub>2</sub> + RO<sub>2</sub> reaction may be responsible for the initial nucleation and growth of SOA. As such, it is conceivable that the ROOR pathway is small relative to RO formation, but a small amount of ROOR may yet contribute to the aerosol formed in the  $\Delta$ carene + NO<sub>3</sub> system, explaining its tendency to nucleate compared to  $\alpha$ -pinene + NO<sub>3</sub>, where highly oxidized monomers are the lowest-volatility species produced in the gas phase. While the Bell et al. 85  $\alpha$ -pinene + NO<sub>3</sub> experiments were conducted at moderate concentrations ( $\sim$ 100 ppb), it is difficult to assess the quantitative importance of the dimers in the SOA formed, since only relative signals were reported and experiments were conducted in the absence of seed (resulting in low aerosol yields). Bates et al.<sup>31</sup> similarly use relative signal contribution in ESI-MS analysis of filter extract to conclude that there are large contributions from dimers in the particle

phase for  $RO_2 + RO_2$  dominated  $\alpha$ -pinene +  $NO_3$  chemistry (also moderate,  $\sim 100$  ppb, concentrations). The SOA analysis methods used in those studies do not allow for identification of ROOR molecules but rather infer their presence by observations of dimer (i.e.,  $C_{17-20}$ ) compounds.

Finally, in the presence of  $HO_2$ , the third major reaction pathway is the  $RO_2 + HO_2$  reaction, with two possible product channels:

$$RO_2 + HO_2 \rightarrow ROOH + O_2$$
 (R3a)

$$\rightarrow$$
 RO + OH + O<sub>2</sub> (R3b)

The  $\mathrm{RO}_2$  +  $\mathrm{HO}_2$  reaction (reaction R3a) typically forms hydroperoxides. The RO pathway (reaction R3b) has been identified to be much more prominent (50% molar yield) with  $\mathrm{RO}_2$  radicals where the alkyl group contains a beta-carbonyl. This case, the first generation chemistry does not have a beta-carbonyl, but rather a beta-nitrooxy functional group, which may similarly cause the  $\mathrm{RO}_2$  +  $\mathrm{HO}_2$  reaction to favor the RO channel over hydroperoxide formation.

In this study, the organic nitrate fraction and AMS spectra showed similar composition for the aerosol formed in the three regimes (Tables 1), and the SOA yields are also quite similar across regimes (Table 1, Figure 4). Given the different products that should dominate these different regimes according to the literature outlined above (RO vs ROOR vs ROOH), the similarities in yield and composition that we observe appear to contradict the idea that there are different major products for different RO<sub>2</sub> fate regimes and require another mechanistic explanation. It is also possible that there are some differences in the detailed composition of the SOA to which the AMS is not sensitive (such as the presence of peroxide functional groups which may thermally decompose before detection, potentially leading to some undercounting of oxygen content if lost as OH or H<sub>2</sub>O; however, this has not been characterized to our knowledge).

Because all three possible bimolecular  $\mathrm{RO}_2$  reactions include the radical pathway producing RO, one potential explanation for the similarity in yields across regimes is that this RO producing channel is in fact major or dominant in all cases. The explanation for the difference in yield across precursors

( $\Delta$ -carene vs  $\alpha$ -pinene) would then be due to differences in subsequent RO chemistry. The prevalence of this RO pathway for the initial oxidation products of both  $\Delta$ -carene + NO<sub>3</sub> and  $\alpha$ -pinene + NO<sub>3</sub> is supported by a recent computational study that was inspired in part by the observations reported here (Kurtén et al., <sup>66</sup> discussed further below).

Another potential explanation for the similarity across regimes could be that RO<sub>2</sub> radicals undergo internal H-abstraction reactions, the so-called "autoxidation" pathway, faster than any bimolecular reaction can take place. <sup>36,66,68,89</sup> Previous studies suggest that autoxidation can be fast and relevant in the atmosphere, by observing highly oxygenated molecules (HOMs) in the field and in the lab using mass spectrometry. <sup>36,89</sup> Some of the HOMs in those studies were of extremely low volatility and had molecular formulas consistent with the presence of hydroperoxyl groups. The researchers suggest that autoxidation formed those HOMs and that the HOMs comprised a considerable portion of SOA mass.

Because autoxidation is a radical propagating process that enables the accumulation of additional hydroperoxide functional groups via  $O_2$  addition, some autoxidation is consistent with the average non-nitrate O/C ratio of ~0.45 observed here for  $\Delta$ -carene; this would be consistent with one -OOH for every 5 carbon atoms. If greater autoxidation is responsible for the higher SOA yields for  $\Delta$ -carene + NO<sub>3</sub>, then we would expect the SOA in those cases to be more oxidized than the  $\alpha$ -pinene + NO<sub>3</sub> experiments; in fact we do observe lower O/C in  $\alpha$ -pinene + NO<sub>3</sub> SOA at modest aerosol loadings, with higher O/C in the earliest condensing SOA (Figures 5 and \$25).

During a subset of these experiments, we monitored gasphase HOMs using NO<sub>3</sub>-CIMS (Figure 6). The major difference observed is a larger fraction of concentration of compounds detected in the  $450-700 \, m/z$  range, where we expect to observe dimers, for  $\Delta$ -carene than for  $\alpha$ -pinene. In addition, the  $\alpha$ -pinene SOA has a greater diversity of monomer-range compounds, whereas the  $\Delta$ -carene monomer region is dominated by two peaks, m/z = 323 and 386, which most likely correspond to (NO<sub>3</sub>)C<sub>10</sub>H<sub>15</sub>NO<sub>7</sub><sup>-</sup> and (NO<sub>3</sub>)- $C_{10}H_{16}N_2O_{10}^-$ , respectively. The former was the largest peak identified by Draper et al.<sup>65</sup> in  $NO_3 + \Delta$ -carene chamber experiments, and the latter was also among the five major monomer peaks detected in that work. Dam et al.90 likewise observed a larger gas-phase yield of dimers for  $\Delta$ -carene than for  $\alpha$ -pinene and observed an anticorrelation of gas-phase O/C ratio with new particle formation number concentrations, supporting the conclusion that high O/C monomers contribute substantially to new particle formation. In contrast to our measurements, they observed approximately half of the total HOMs signal in the dimer region (see Figure 4 in their paper), where we observed on the order of  $\sim$ 1%. It is unclear what contributed to those differences, but we note that these experiments had very different chemical conditions, since the Dam et al. experiments were conducted in a continuous flowthrough mode where NO3 was generated in situ and monoterpenes were steadily injected (see more discussion in section 3.4 below). The HOMs measurements and modeling conducted as part of this study is described in more detail in section 3.4 below.

An additional piece of evidence that helps constrain the  $RO_2$  fate kinetics is the rapid rate at which SOA is formed when immediately reacting 100/10 ppb of  $N_2O_5$  with 10/100 ppb of terpene. While yields were typically recorded at  $\sim 10-15$  min,

typical time scales observed for SOA to rise toward peak mass concentrations was  $\sim 200$  s (one e-fold). In the case of the RO<sub>2</sub> + NO<sub>3</sub> fate experiments (100 ppb N<sub>2</sub>O<sub>5</sub>, 10 ppb terpene), the remaining  $N_2 \tilde{O}_5$  available ( $\sim 90~\text{ppb}$ ) can react rapidly with the ~10 ppb RO<sub>2</sub> (e-fold ~6 s for lifetime of RO<sub>2</sub> reaction with NO<sub>3</sub>). Therefore, that reaction is not expected to have much effect on the overall rate of SOA formation. However, for the  $RO_2 + RO_2$  fate experiments (10 ppb  $N_2O_5$ , 100 ppb terpene), the rapid SOA rise allows for estimation of the minimum RO2 + RO<sub>2</sub> rate coefficient, under the assumption that the reaction is a rate-limiting step to formation of the major condensing products. Additional contributions to the ~200 s time scale of SOA formation include the fast reaction of NO<sub>3</sub> with the terpene (and replenishment of NO<sub>3</sub> from N<sub>2</sub>O<sub>5</sub> decomposition) as well as the phase transformations of condensation and evaporation with particles and walls. Typical particle condensational rate coefficients for nonseeded  $\Delta$ -carene experiments rapidly rose and peaked at 0.02-0.06 s<sup>-1</sup> (15-50 s condensing lifetime). In the vapor fate modeling (which explicitly accounts for phase transformation kinetics and the initial terpene + NO<sub>3</sub> reaction), it was found that an additional time delay coefficient of 0.01 s<sup>-1</sup> (100 s time scale) was required to represent the SOA formation (see section \$1.3), which may be attributed to some combination of the remaining factors that may control the SOA formation kinetics, such as the time for RO<sub>2</sub> to form condensable products, terpene injection time, and mixing. Thus, assuming some contribution for the latter two factors, we take 60 s as the maximum time for the initial RO<sub>2</sub> to form the major condensing products. This equates to a lower limit of the  $RO_2 + RO_2$  rate coefficient of  $7.1 \times 10^{-14}$  cm<sup>3</sup> molec s<sup>-1</sup>. This value is approximately threefifths toward the upper limit rate coefficient (on a logarithmic scale) for the range shown by the two bounding-case ternary plots in Figure 3, and because this is a rough estimation and a lower limit, the rate coefficient may be even faster. This is similar to the bulk RO<sub>2</sub> + RO<sub>2</sub> rate coefficient estimated by Bates et al.<sup>31</sup> for RO<sub>2</sub> produced from  $\alpha$ -pinene + NO<sub>3</sub> reactions, using approximate observational constraints involving comparison to competing RO<sub>2</sub> + NO<sub>3</sub>/HO<sub>2</sub> reactions. However, this does not rule out the possibility of other equal or faster reactions of the initial RO2 occurring that lead to the main condensable products within a ~1 min time frame. For comparison, the lower limit rate coefficient (2  $\times$  10<sup>-15</sup> cm<sup>3</sup> molec s<sup>-1</sup>) corresponds to an RO<sub>2</sub> reaction time scale of 2100 s, an order of magnitude longer than the typical observed SOA formation time scale. As discussed earlier, for the upper bound rate coefficient of  $1 \times 10^{-12}$  cm<sup>3</sup> molec s<sup>-1</sup> shown in the right panel of Figure 3 (and which appears to be more representative than the lower limit based on evidence presented here), the range of experiments conducted here would have represented all three RO<sub>2</sub> fate regimes, if only considering the initial reactions with RO<sub>2</sub>, NO<sub>3</sub> and HO<sub>2</sub>.

Based on the totality of the experimental evidence reported here, and informed by recent computational studies illuminating the rates of autoxidation reactions specific to these monoterpene structures,  $^{65,66}$  the true explanation for the SOA yield similarity across RO $_2$  fate regimes in  $\Delta\text{-carene}$  + NO $_3$  is likely due to initial RO formation and subsequent similar chemistry. The pervasive and consistent formation of oligomers in the particle phase may also contribute to the similarity of yields.  $^{43,45,73}$  The high O/C measured by the AMS in all regimes and for both precursors suggests that multiple oxygen additions to the monoterpene backbone must occur

before the molecule partitions to the particle phase. These oxygen additions can typically occur through autoxidation or RO isomerization, or both. Kurtén et al. 66 predict that neither of the initially formed nitrato-RO2 radicals from  $\Delta$ -carene + NO3 nor  $\alpha$ -pinene + NO3 would undergo RO2 autoxidation reactions at typical atmospheric (or our chamber) conditions; the rates of the intramolecular rearrangements are not sufficiently rapid to outcompete bimolecular reactions. Instead, the bimolecular reactions could produce RO radicals in both cases, and it is the difference in the fate of these *alkoxy* radicals that causes the difference in SOA yields among terpenes.

In the  $\Delta$ -carene case, the RO undergoes a scission reaction that causes ring-opening and leaves a reactive carbon radical that can quickly become an RO<sub>2</sub> radical. This RO-isomerization-produced, ring-opened nitrato-RO<sub>2</sub> now has limited kinetically accessible autoxidation reactions, as well as the possibility to undergo any of the bimolecular reactions (reactions R1-R3) discussed above, potentially with different product branching ratios than the initially produced RO<sub>2</sub>. The dimers observed in the  $\Delta$ -carene NO<sub>3</sub>-CIMS spectra are likely products of reaction R2c, possibly from autoxidized RO<sub>2</sub>; however, they contribute only a small fraction to the total HOMs observed.

However, in the  $\alpha$ -pinene case, the thermodynamically favored RO scission reaction breaks a different bond and results primarily in the loss of the NO<sub>2</sub> group and production of the volatile product pinonaldehyde. This explains the overall lower SOA yield from  $\alpha$ -pinene + NO<sub>3</sub>. The smaller amount of aerosol that is produced is more semivolatile, as shown in Figure 4, with less oxygen, possibly shorter carbon chain and even less prone to be dimerized in the gas phase (Figure 6).

In summary, an explanation consistent with our results is that the structures of the monoterpenes  $\alpha$ -pinene and  $\Delta$ -carene themselves cause divergent alkoxy-radical mediated product channels which in one case enable multigenerational reactions ( $\Delta$ -carene) and in the other shuttle a much larger fraction of the precursor to volatile products ( $\alpha$ -pinene), leaving smaller product channels to produce SOA at moderate OA concentrations.

3.3.1. Further Discussions of H-Shift Reactions and Autoxidation. Here, we provide additional discussion supporting and summarizing our conclusion that autoxidation is unlikely to be a major route to forming condensable material for these systems. As discussed in section 3.2.3, the SOA produced in an experiment conducted under typical RO<sub>2</sub> +  $RO_2$  regime conditions for  $\Delta$ -carene was analyzed and shown to contain only a small amount of peroxide functional groups (7% of the non-nitrate oxygen content). As discussed above in this section and section 2.5, Kurtén et al.<sup>66</sup> showed that H-shift reactions of the initially formed RO<sub>2</sub> is improbable, while Draper et al. 65 expanded on that analysis showing that for subsequent RO2 radicals, the only H-shift reactions that could compete with bimolecular reactions are those involving alpha hydrogens associated with the nitrate group carbon adjacent to a carbonyl group. Calculated rates were  $5.4-8.0 \times 10^{-2} \text{ s}^{-1}$  for the two likely RO<sub>2</sub> reactants considered and leads to the loss of NO<sub>2</sub>, forming dicarbonyl hydroperoxides that terminate the reactions. Therefore, if these H-shift reactions were competitive and the products partitioned to the aerosols, then substantial peroxide content should have been detected in our analysis. In contrast, if those products remained dominantly in the gas phase, then we would not expect to have observed

them. While organic hydroperoxides are known to be susceptible to decomposition, studies have shown a relatively consistent rate of ~15% hr<sup>-1</sup> in the absence of acid seed. For our peroxide analysis, samples were collected for 2.5 h and then immediately extracted (after which decomposition should be slow), thus overall losses should have been modest (<15–30%). We note that in a previous study of  $\alpha$ -pinene ozonolysis under autoxidation conditions, using the same methods, 1.0 peroxide group per  $C_{10}$  monomer was measured in the aerosol (compared to 0.14 in this study).

Another aspect to consider regarding the likelihood of autoxidation are comparisons of the rates of H-shift abstraction versus bimolecular reactions. As noted above, the largest Hshift rate coefficients for  $\Delta$ -carene oxidation calculated by Draper et al.<sup>65</sup> were  $5.4-8.0 \times 10^{-2}$  s<sup>-1</sup>. Based on measured SOA formation rates for that reaction in the RO<sub>2</sub> + RO<sub>2</sub> regime (discussed earlier in this section), and a minimum time scale for forming all condensing products of 60 s, we estimated a lower limit for the  $RO_2 + RO_2$  rate coefficient of  $7.1 \times 10^{-14}$ cm<sup>3</sup> molecule  $s^{-1}$ . Thus, the ~15 s time scale predicted by Draper et al.<sup>65</sup> for those reactions may be competitive with RO<sub>2</sub> + RO<sub>2</sub> reactions for our conditions. The fact that we do not observe substantial peroxide content may be due to faster  $RO_2 + RO_2$  rates than our lower limit estimate, overestimation of the H-shift rate coefficients, or because the peroxide products do not partition to the aerosol.

Since we only conducted the peroxide analysis for the RO<sub>2</sub> + RO<sub>2</sub> system, we similarly consider the competitiveness of the rates for the  $RO_2 + NO_3$  and  $RO_2 + HO_2$  experiments. For our nominal RO<sub>2</sub> + NO<sub>3</sub> experiments, kinetic modeling predicts that reaction with NO3 would be 2 times faster than the Hshift reaction. In contrast, for our nominal RO<sub>2</sub> + HO<sub>2</sub> experiments, kinetic modeling predicts that reaction with HO<sub>2</sub> would be 2-4 times slower than the H-shift reaction (for the range of  $N_2O_5$  injection rates used of 1.5–0.15 ppb min<sup>-1</sup>, respectively). The difference between the NO<sub>3</sub> versus HO<sub>2</sub> experiments is because, despite the order of magnitude faster rate coefficient for reaction with RO2, the HO2 concentrations sustained during the oxidation period are substantially lower than NO<sub>3</sub> concentrations. Thus, by comparison to the RO<sub>2</sub> + RO<sub>2</sub> experiment with comparable estimated bimolecular reaction rates (assuming the 60 s RO<sub>2</sub> lifetime is representative) and observation of little peroxide contributions for those conditions, it appears unlikely that autoxidation was important for the RO<sub>2</sub> + NO<sub>3</sub> and RO<sub>2</sub> + HO<sub>2</sub> experiments. However, given the constraints available for these rate comparisons discussed, the RO2 + HO2 experiments have the most likely conditions for the H-shift reactions to be competitive. Nevertheless, if all the RO2 radicals formed the Hshift products that Draper et al.65 highlighted, then the dicarbonyl hydroperoxides would likely be too volatile ( $C^* \sim$ 380  $\mu$ g m<sup>-3</sup>; estimated per Pankow and Asher)<sup>93</sup> to substantially condense to the particle phase (6% at OA of 25  $\mu$ g m<sup>-3</sup>) and therefore would make only a minor contribution to SOA yields measured here.

For typical nighttime conditions in biogenic-VOC-rich environments, the autoxidation rates considered in Draper et al. may be more competitive with bimolecular RO $_2$  reactions. For example, considering typical HO $_2$  concentrations of 5 ppt, 4 (as used in Figure 3), using the rate coefficients in Table S6, the lifetime of RO $_2$  for reaction with HO $_2$  would be ~500 s, compared to the ~15 s lifetimes computed by Draper et al. For typical nighttime values of ~1 ppt for NO $_3$  and RO $_2$ 

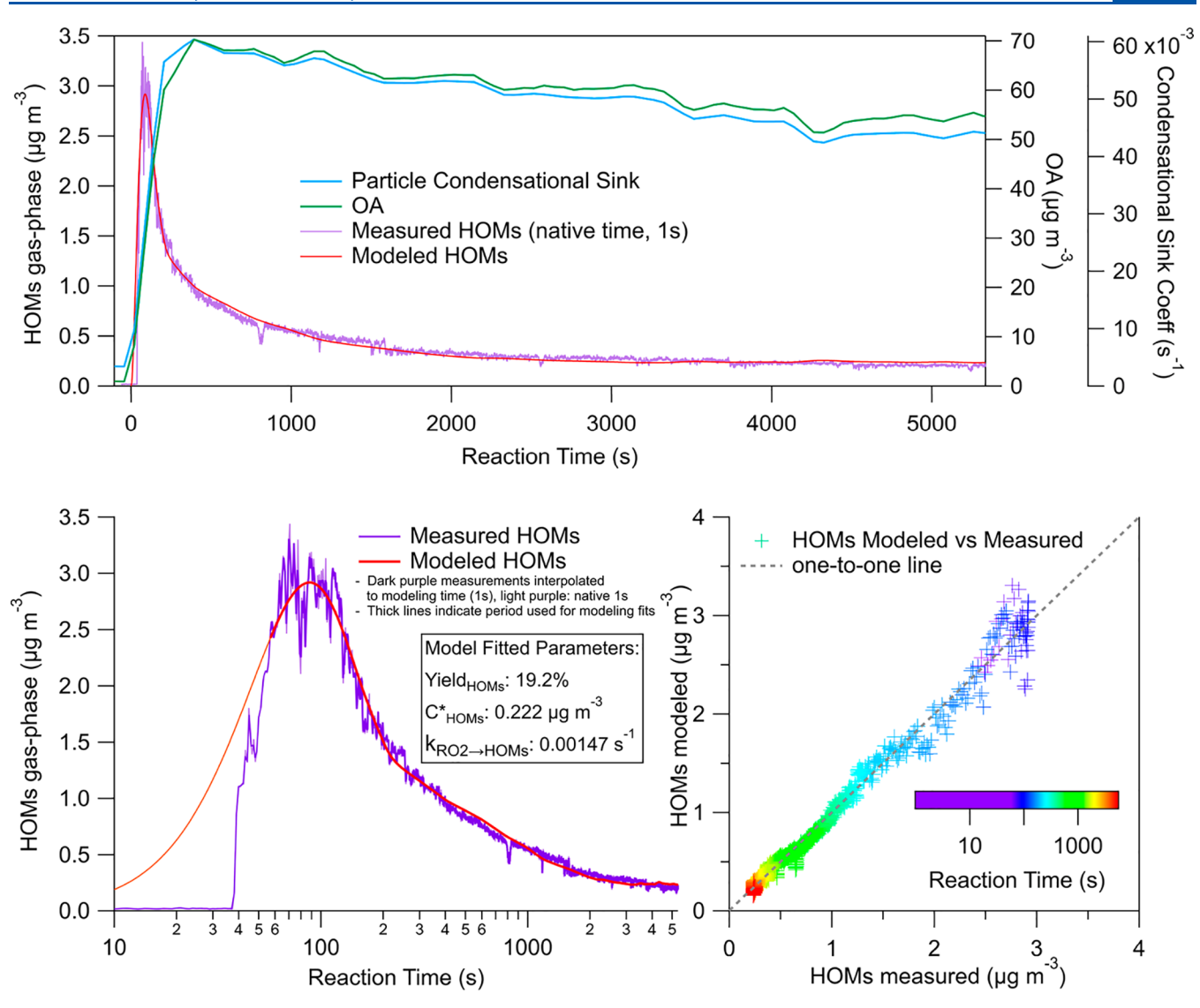


Figure 7. HOMs measured and modeled time series shown as linear (a) and log (b) time axes and as a scatter plot (c). Particle condensational sink rate coefficient and OA concentrations are also shown in panel a.

concentrations 3-fold higher than  $HO_2$  (and assuming the upper limit  $RO_2 + RO_2$  rate coefficient of  $1 \times 10^{-12}$  cm³ molecule<sup>-1</sup> s<sup>-1</sup>), reaction with  $NO_3$  and  $RO_2$  would be ~50 and ~7 times slower than with  $HO_2$ , respectively. However, given the high volatility of the product compounds expected, those H-shift reactions would produce very little aerosol under typical ambient conditions. Therefore, faster H-shift reactions at later reaction steps would be required for autoxidation to play a substantial role in ambient SOA formation from this system, which we do not observe evidence for in our  $RO_2$  +  $RO_2$  experiments nor did DeVault et al. <sup>73</sup>

**3.4.** Highly Oxidized Molecule Measurements and Modeling. The time series of the measurements of HOMs from a  $\Delta$ -carene oxidation experiment (experiment 24) was modeled, in order to estimate the ensemble HOMs yield, volatility, and production rate. The ensemble HOMs concentration was treated as a single entity for the purposes of this simplified demonstration. Calibrated concentrations of the time evolution is shown in Figure 7. Concentrations rapidly rise in  $\sim$ 25 s, reach a peak for 50–100 s, decrease rapidly for 50–100 s, and then more gradually decay over thousands of seconds. A chemistry/vapor fate modeling

scheme, similar to that described above (section 2.4), was used for the HOMs modeling. The difference is that only the evolution of HOMs was tracked, where the chemistry only consisted of  $\Delta$ -carene oxidation by NO<sub>3</sub> forming RO<sub>2</sub>, followed by a generalized reaction step,  $RO_2 \rightarrow HOMs$ . Similarly, the partitioning of HOMs between gas phase and either particles or chamber walls, as well as irreversible particle loss, is tracked. Particle OA concentrations and condensational sink are constrained to bulk particle-phase observations. An average molecular weight of 325 g mol-1 was used for condensational sink calculations and concentration conversions. Like for the evaporation modeling (see section \$3.0), the model was run iteratively using a fitting function to optimize key parameters. Those fitted parameters here include three values: the HOMs yield, volatility, and the  $RO_2 \rightarrow HOMs$  rate coefficient. In order to obtain good measurement-modeling agreement, the HOMs concentration timestamp was adjusted so that the measurement and modeling peaks aligned, and the rapid rise was not included in the fitting optimization (see Figure 7). The need for such treatment is likely due to the uncertainties at approximately minute time scales associated with nondiscrete addition of terpene precursor, chamber

mixing, and the relatively slow time resolution of SMPS measurements (that track a rapidly increasing condensational sink). Differences in results when excluding these adjustments or sensitivities to time alignment are discussed below.

The optimized HOMs model temporal profile, compared to the measurements, is shown in Figure 7. The optimized parameters are yield<sub>HOMs</sub>: 19.2  $\pm$  0.1%,  $C^*_{HOMs}$ : 0.222  $\pm$  0.003  $\mu g \text{ m}^{-3}$ ,  $k_{\text{RO}_2 \to \text{HOMs}}$ : 0.00147  $\pm$  0.00001 s<sup>-1</sup>. The uncertainty listed represents the 95% confidence interval of the fit and does not reflect overall uncertainties. The yield is similar to the  $C^*$  = 1  $\mu$ g m<sup>-3</sup> yield from the overall yield fitting with vapor fate corrections (Figures 4, S20, and S22). The fitted volatility is four and half times lower than the prescribed  $C^* = 1 \mu \text{g m}^{-3}$ volatility bin used for the overall SOA yield fitting, which reflects that neither the yield fitting nor evaporation modeling provide adequate constraints to quantitatively separate the VBS below  $C^* = 1 \mu \text{g m}^{-3}$ . In contrast, the HOMs modeling here, suggests that a large portion of the bulk yield-fitted  $C^*=1$  $\mu$ g m<sup>-3</sup> bin is of substantially lower volatility. This distinction could be important for modeling SOA in some regions, depending on their OA concentrations.

This overall yield (19% by mass) is orders of magnitude larger than reported by Dam et al., 90 who reported molar yields of 2.5  $\times$  10<sup>-4</sup> % for total HOMs produced from reaction of  $\Delta$ carene and NO<sub>3</sub>, also using a NO<sub>3</sub>-CIMS to detect gas-phase. While their experiments were conducted in a different type chamber (560 L stainless-steel chamber), wall loss corrections for the HOMs, based on tests where oxidation was stopped and started, were applied. Additionally, the calibration factor used for computing HOMs concentrations for that analysis was similar to that used here. However, gas-particle interactions were not evaluated in the Dam et al. study, which could potentially be a major factor in the lower yields, especially in context of using continuous flow-through mode where the ratio of gas-phase production to losses could be greatly reduced (thus lowering HOMs concentrations) compared to the fast-burst oxidation method used here. For example, for the modeling conducted here, where nearly all the oxidation occurs on a short time scale of on the order of a minute (and also particle condensational sink is initially low), the peak HOMs gas-phase concentrations observed (Figure 7) still only reaches  $\sim$ 5% of the total HOMs produced. For the Dam et al. study, the equivalent concentration of ~41 ppb of monoterpenes was steadily injected over the ~31 min residence time of the reaction chamber (in the presence of nucleated particles). In contrast, Shen et al. 96 reported mass yields of total organic nitrate HOMs (also detected with NO<sub>3</sub>-CIMS) of 12.5% (-6.8%/+14.6%) from  $\beta$ -pinene + NO<sub>3</sub>, very similar to our observations of total HOMs from  $\Delta$ -carene. That study was conducted in a large (~270 m³) chamber, run in batch mode, without seed nor significant particle formation, and with 0.1-5ppbv  $N_2O_5$  and terpene concentrations.

The fitted  $RO_2 \rightarrow HOMs$  rate coefficient ( $k_{RO_2 \rightarrow HOMs}$ ) is slower than expected, representing a time scale of ~700 s, which is substantially slower than typical time scales observed for SOA to reach peak mass concentrations (~200 s for an efold). Once substantial particle formation and/or substantial particle growth occurs for the  $\Delta$ -carene experiments, gastoparticle condensation time scales are typically tens of seconds, and the reaction of  $\Delta$ -carene with  $NO_3$  occurs in ~25 s. The remainder of the time-limiting steps for bulk particle mass formation include a convolution of the time to build up

substantial particle concentrations, injection/mixing times, and the subsequent reaction(s) of the initial  $RO_2$  to form condensable compounds. It might be expected that HOMs formation may play an important role in the new-particle formation commonly observed upon initial reaction of  $\Delta$ -carene with  $NO_3$ , thus occurring on time scales as fast or faster than the bulk particle mass formation and condensational sink rise. However, that process may not require formation of large concentrations of HOMs. Moreover, treating the ensemble of HOMs as one entity for this modeling is clearly a simplification, while the bulk time series is composed of many different compounds that may have distinct yields, volatility and formation rates.

Nonetheless, the time profile supports a sustained production of HOMs on the longer time scale. Prescribing a much faster time  $k_{\rm RO_2 \rightarrow HOMs}$  in the model (0.1–0.01 s<sup>-1</sup>) results in a rapid rise in HOMs concentrations (with better fit to the steep rise and much lower yields), however with a rapid decrease in concentrations, reaching relatively constant concentrations within 100-200 s, and thus very poor measurement-modeling match for the ~200-2000 s period. This highlights that the bulk  $k_{\text{RO}_2 \rightarrow \text{HOMs}}$  largely controls the shape of the 200-1000 s period of the HOMs time profile. The shape and magnitude of the early peak (<200 s) is largely controlled by the interplay of the  $k_{RO,\rightarrow HOMs}$ , yield, and particle condensational sink, while the gas-phase concentrations at longer time scales (thousands of seconds) are controlled by the HOMs yield, volatility, and OA concentrations, as the HOMs are in a pseudo steady state between gas and particle phases. The approach to equilibrium between gas-phase with the chamber walls occurs on several thousands of seconds time scales (gas-wall/gas ratio is 6.4 at 5000 s as it approaches an expected equilibrium ratio of 9.5, according to the fitted parameters), which is much longer than the gas  $\rightarrow$  wall  $\sim$ 1000 s rate coefficient, since only a small portion of the HOMs formed are present in the gas-phase, thus slow particle-phase evaporation limits transfer to walls. For example, at 2000 s, the model predicts that 0.5%/96%/2.0%/1.9% are in the gas/ particle/wall/particle-wall phases, respectively. The dominant contributors to uncertainties in the modeled HOMs yield is likely due to the particle condensational sink estimation  $(\pm 25\%)$  and the HOMs calibration (at best,  $\pm 25\%$ ), therefore  $\pm 35\%$  or higher overall. Additionally, the sensitivity to the time alignment of SMPS (a 3 min scan) was tested by adjusting the condensational sink and OA timestamps forward/backward 1 min. Resulting fits of yield<sub>HOMs</sub>,  $C^*_{HOMs}$ , and  $k_{RO_2 \to HOMs}$  were +14%/-7%, -33%/+22%, and -45%/+53% compared to the base fits, respectively. Conducting experiments with substantial concentrations of organic seed particles present prior to the rapid oxidation, would reduce sensitivity to time alignment of slower particle-phase measurements.

3.5. Slow/No Hydrolysis of Organic Nitrates. Several laboratory and modeling studies have measured or inferred the degree, rates, or importance of hydrolysis of particle phase organic nitrate, which may depend on various factors such as the precursor, oxidants, nitrate functional group degree of substitution, or particle acidity or water content. Recent laboratory studies found these lifetimes to be quite short in the case of  $\alpha$ -pinene and  $\beta$ -pinene + NO<sub>3</sub> (30 min), albeit for a small hydrolyzable fraction of the total organic nitrates produced in each case (9–17% and 9–15%, respectively). <sup>41</sup> Therefore, a few of the present SOA experiments were

conducted at elevated RH, with neutral ammonium sulfate seed aerosol, in order to investigate the hydrolysis of the organic nitrates in the SOA produced. No significant (>10–15%) hydrolysis of  $\Delta$ -carene derived organic nitrate in these high-RH experiments was observed on the time scale of these experiments (Figure S26). This is consistent with the results reported by Takeuchi and Ng<sup>41</sup> for ( $\beta$ -pinene + NO<sub>3</sub>)-derived SOA and not unexpected given that the structures of both  $\beta$ -pinene and  $\Delta$ -carene, and the tendency of radical attack to favor the most substituted peroxy radical product should result in the dominance of nontertiary organic nitrate functional groups.

# 4. IMPLICATIONS AND CONCLUSIONS

The observation of similar SOA mass yields across varying  $RO_2$  fate regimes for  $\Delta$ -carene and  $\alpha$ -pinene, initiated by reaction with nitrate radicals, is an indication that (at least for these two monoterpenes) these chamber data can be taken to be representative of the real atmosphere, even when collected under conditions that feature higher than atmospheric concentrations of  $HO_2$ ,  $RO_2$ , and  $NO_3$ . Instead, atmospheric relevance of chamber data is likely more driven by total concentrations of precursors, organic aerosol loading and proper accounting for chamber wall effects on SOA-relevant gases.

The OA dependence of SOA formation from  $\alpha$ -pinene + NO<sub>3</sub> is perhaps not too surprising and explains the seemingly disparate yields reported in the literature. Taken together with the generally small SOA yields and anticorrelation of O/C with OA, this is consistent with the  $\alpha$ -pinene-derived SOA arising from the more-oxidized semivolatile products of a minor reaction pathway, while that from  $\Delta$ -carene comes from major reaction pathways that produce molecules with substantially lower volatility, due to the contributions of multigenerational reactions and particle-phase dimer formation.

The marked and robust regime-independent difference in SOA yield from two different precursor monoterpenes suggests that in order to accurately model SOA production in forested regions, the chemical mechanism must feature speciated monoterpenes. With SOA yields from  $\Delta$ -carene being substantially larger than  $\alpha$ -pinene, we can infer that NO<sub>3</sub>-initiated terpene SOA production may be more efficient in regions with greater relative  $\Delta$ -carene emissions, such as the Pacific Northwest. In regions dominated by the lower SOA yielding  $\alpha$ -pinene, nighttime oxidation may instead produce gas-phase reaction products that could affect daytime SOA and/or ozone production.

#### ASSOCIATED CONTENT

#### Supporting Information

The Supporting Information is available free of charge at https://pubs.acs.org/doi/10.1021/acs.jpca.2c04419.

Experimental setup diagram. Discussion of  $\Delta$ -carene isomers. Individual experiment conditions and results. Reactions and rate coefficients for kinetic modeling and particle-wall loss calculations/corrections. SOA yield curves. Calculation of density, pRONO<sub>2</sub> contributions, elemental ratios, relative ionization efficiency, and collection efficiency of SOA. Methods and results for iterative approach to yield curve fitting, VBS derivation, and vapor wall-effects modeling and yield correction factors (including for different pre-existing SOA

assumptions). Methods and results for compound fate modeling of vapor-phase wall losses using SOA evaporation profiles for  $\Delta$ -carene. AMS mass spectra. Time series of experiments for hydrolysis loss of pRONO<sub>2</sub>. (PDF)

# AUTHOR INFORMATION

#### **Corresponding Authors**

Douglas A. Day — Department of Chemistry and Cooperative Institute for Research in Environmental Sciences, University of Colorado Boulder, Boulder, Colorado 80309, United States; orcid.org/0000-0003-3213-4233; Phone: 303-492-9599; Email: douglas.day@colorado.edu

Juliane L. Fry — Department of Chemistry, Reed College, Portland, Oregon 97202, United States; Present Address: Department of Environmental Sciences, Wageningen University, 6708 PB Wageningen, Netherlands; orcid.org/0000-0003-1799-5828; Phone: +31-317-487754; Email: juliane.fry@wur.nl

Jose L. Jimenez — Department of Chemistry and Cooperative Institute for Research in Environmental Sciences, University of Colorado Boulder, Boulder, Colorado 80309, United States; orcid.org/0000-0001-6203-1847; Phone: 303-492-3557; Email: jose.jimenez@colorado.edu

#### **Authors**

Hyun Gu Kang — Department of Chemistry and Cooperative Institute for Research in Environmental Sciences, University of Colorado Boulder, Boulder, Colorado 80309, United States; Department of Chemistry, Reed College, Portland, Oregon 97202, United States; Present Address: Center for Environment, Health, and Welfare Research Korea Institute for Science and Technology 02792 Seoul, South Korea; orcid.org/0000-0002-3320-9447

Jordan E. Krechmer – Department of Chemistry and Cooperative Institute for Research in Environmental Sciences, University of Colorado Boulder, Boulder, Colorado 80309, United States; Present Address: Aerodyne Research, Inc., 45 Manning Rd., Billerica, MA 01821, United States; orcid.org/0000-0003-3642-0659

Benjamin R. Ayres — Department of Chemistry, Reed College, Portland, Oregon 97202, United States; Present Address: Oregon Department of Environmental Quality, Portland, OR 97232, United States

Natalie I. Keehan – Department of Chemistry, Reed College, Portland, Oregon 97202, United States

Samantha L. Thompson – Department of Chemistry and Cooperative Institute for Research in Environmental Sciences, University of Colorado Boulder, Boulder, Colorado 80309, United States

Weiwei Hu — Department of Chemistry and Cooperative Institute for Research in Environmental Sciences, University of Colorado Boulder, Boulder, Colorado 80309, United States; Present Address: State Key Laboratory at Organic Geochemistry, Guangzhou Institute of Geochemistry, Chinese Academy of Sciences, Guangzhou 510640, China; orcid.org/0000-0002-3485-6304

Pedro Campuzano-Jost — Department of Chemistry and Cooperative Institute for Research in Environmental Sciences, University of Colorado Boulder, Boulder, Colorado 80309, United States; orcid.org/0000-0003-3930-010X

**Jason C. Schroder** – Department of Chemistry and Cooperative Institute for Research in Environmental Sciences,

- University of Colorado Boulder, Boulder, Colorado 80309, United States
- Harald Stark Cooperative Institute for Research in Environmental Sciences, University of Colorado Boulder, Boulder, Colorado 80309, United States; Aerodyne Research Inc., Billerica, Massachusetts 01821, United States; orcid.org/0000-0002-0731-1202
- Marla P. DeVault Department of Chemistry and Cooperative Institute for Research in Environmental Sciences, University of Colorado Boulder, Boulder, Colorado 80309, United States
- Paul J. Ziemann Department of Chemistry and Cooperative Institute for Research in Environmental Sciences, University of Colorado Boulder, Boulder, Colorado 80309, United States; orcid.org/0000-0001-7419-0044
- Kyle J. Zarzana Cooperative Institute for Research in Environmental Sciences, University of Colorado Boulder, Boulder, Colorado 80309, United States; Chemical Sciences Laboratory, National Oceanic & Atmospheric Administration, Boulder, Colorado 80305, United States; Present Address: Department of Chemistry, University of Colorado Boulder, Boulder, CO 80309, United States; orcid.org/0000-0003-1581-6419
- Robert J. Wild Cooperative Institute for Research in Environmental Sciences, University of Colorado Boulder, Boulder, Colorado 80309, United States; Chemical Sciences Laboratory, National Oceanic & Atmospheric Administration, Boulder, Colorado 80305, United States; Present Address: Institute for Ion Physics and Applied Physics, University of Innsbruck, Innsbruck 6020, Austria
- William P. Dubè Cooperative Institute for Research in Environmental Sciences, University of Colorado Boulder, Boulder, Colorado 80309, United States; Chemical Sciences Laboratory, National Oceanic & Atmospheric Administration, Boulder, Colorado 80305, United States
- Steven S. Brown Chemical Sciences Laboratory, National Oceanic & Atmospheric Administration, Boulder, Colorado 80305, United States; Department of Chemistry, University of Colorado Boulder, Boulder, Colorado 80309, United States; ocid.org/0000-0001-7477-9078

Complete contact information is available at: https://pubs.acs.org/10.1021/acs.jpca.2c04419

#### **Author Contributions**

\*D.A.D. and J.L.F. contributed equally to this work.

The authors declare no competing financial interest.

# ACKNOWLEDGMENTS

This research was supported by NOAA's Climate Program Office's Atmospheric Chemistry, Carbon Cycle, and Climate program grant nos. NA13OAR4310070 and NA18OAR4310113, and US NSF grants AGS-1740610 and AGS-1822664. J.L.F. also received funding through the United States Environmental Protection Agency (EPA) National Center for Environmental Research's (NCER) Science to Achieve Results (STAR) program grant no. RD-83539901. This article has not been formally reviewed by the EPA, and the views expressed in this document are solely those of the authors and do not necessarily reflect those of the EPA. The EPA does not endorse any products or commercial services mentioned in this publication. The authors thank D. Pagonis,

M. Claflin, L. Algrim, A. Ranney, and P. Handley for their help conducting the chamber experiments.

#### REFERENCES

- (1) Goldstein, A. H.; Galbally, I. Known and Unexplored Organic Constituents in the Earth's Atmosphere. *Environ. Sci. Technol.* **2007**, 41 (5), 1514–1521.
- (2) Jimenez, J. L.; Canagaratna, M. R.; Donahue, N. M.; Prevot, A. S. H.; Zhang, Q.; Kroll, J. H.; DeCarlo, P. F.; Allan, J. D.; Coe, H.; Ng, N. L.; et al. Evolution of Organic Aerosols in the Atmosphere. *Science* **2009**, 326 (5959), 1525–1529.
- (3) Hallquist, M.; Wenger, J. C.; Baltensperger, U.; Rudich, Y.; Simpson, D.; Claeys, M.; Dommen, J.; Donahue, N. M.; George, C.; Goldstein, A. H.; et al. The Formation, Properties and Impact of Secondary Organic Aerosol: Current and Emerging Issues. *Atmos. Chem. Phys.* **2009**, *9*, 5155–5236.
- (4) Hodzic, A.; Campuzano-Jost, P.; Bian, H.; Chin, M.; Colarco, P. R.; Day, D. A.; Froyd, K. D.; Heinold, B.; Jo, D. S.; Katich, J. M.; et al. Characterization of Organic Aerosol across the Global Remote Troposphere: A Comparison of ATom Measurements and Global Chemistry Models. *Atmos Chem. Phys.* **2020**, *20* (8), 4607–4635.
- (5) Goldstein, A. H.; Koven, C. D.; Heald, C. L.; Fung, I. Y. Biogenic Carbon and Anthropogenic Pollutants Combine to Form a Cooling Haze over the Southeastern United States. *Proc. Natl. Acad. Sci. U. S. A.* **2009**, *106* (22), 8835–8840.
- (6) Myhre, G.; Samset, B. H.; Schulz, M.; Balkanski, Y.; Bauer, S.; Berntsen, T. K.; Bian, H.; Bellouin, N.; Chin, M.; Diehl, T.; et al. Radiative Forcing of the Direct Aerosol Effect from AeroCom Phase II Simulations. *Atmos Chem. Phys.* **2013**, *13* (4), 1853–1877.
- (7) Murray, C. J. L.; Aravkin, A. Y.; Zheng, P.; Abbafati, C.; Abbas, K. M.; Abbasi-Kangevari, M.; Abd-Allah, F.; Abdelalim, A.; Abdollahi, M.; Abdollahpour, I.; et al. Global Burden of 87 Risk Factors in 204 Countries and Territories, 1990–2019: A Systematic Analysis for the Global Burden of Disease Study 2019. *Lancet* 2020, 396 (10258), 1223–1249.
- (8) Pope, C. A.; Coleman, N.; Pond, Z. A.; Burnett, R. T. Fine Particulate Air Pollution and Human Mortality: 25+ Years of Cohort Studies. *Environ. Res.* **2020**, *183*, 108924.
- (9) Romley, J. A.; Hackbarth, A.; Goldman, D. P. The Impact of Air Quality on Hospital Spending. *Rand Health Q.* **2012**, *2* (3), 6.
- (10) Sheffield, P.; Roy, A.; Wong, K.; Trasande, L. Fine Particulate Matter Pollution Linked to Respiratory Illness in Infants and Increased Hospital Costs. *Health Aff. Proj. Hope* **2011**, 30 (5), 871–878
- (11) Guenther, A.; Hewitt, C. N.; Erickson, D.; Fall, R.; Geron, C.; Graedel, T.; Harley, P.; Klinger, L.; Lerdau, M.; McKay, W. A.; et al. Global Model of Natural Volatile Organic Compound Emissions. *J. Geophys Res.* 1995, 100, 8873–8892.
- (12) Spracklen, D. V.; Jimenez, J. L.; Carslaw, K. S.; Worsnop, D. R.; Evans, M. J.; Mann, G. W.; Zhang, Q.; Canagaratna, M. R.; Allan, J.; Coe, H.; et al. Aerosol Mass Spectrometer Constraint on the Global Secondary Organic Aerosol Budget. *Atmos. Chem. Phys.* **2011**, *11* (23), 12109–12136.
- (13) Guenther, A.; Jiang, X.; Heald, C. L.; Sakulyanontvittaya, T.; Duhl, T.; Emmons, L. K.; Wang, X. The Model of Emissions of Gases and Aerosols from Nature Version 2.1 (MEGAN2.1): An Extended and Updated Framework for Modeling Biogenic Emissions. *Geosci. Model Dev.* 2012, 5 (6), 1471–1492.
- (14) Kulmala, M.; Vehkamäki, H.; Petäjä, T.; Dal Maso, M.; Lauri, A.; Kerminen, V.-M.; Birmili, W.; McMurry, P. H. Formation and Growth Rates of Ultrafine Atmospheric Particles: A Review of Observations. *J. Aerosol Sci.* **2004**, *35* (2), 143–176.
- (15) Heald, C. L.; Henze, D. K.; Horowitz, L. W.; Feddema, J.; Lamarque, J.-F.; Guenther, A.; Hess, P. G.; Vitt, F.; Seinfeld, J. H.; Goldstein, A. H. Predicted Change in Global Secondary Organic Aerosol Concentrations in Response to Future Climate, Emissions, and Land Use Change. *J. Geophys. Res. Atmospheres* **2008**, *113*, D05211.

- (16) Peñuelas, J.; Staudt, M. BVOCs and Global Change. *Trends Plant Sci.* **2010**, *15* (3), 133–144.
- (17) Kourtchev, I.; Giorio, C.; Manninen, A.; Wilson, E.; Mahon, B.; Aalto, J.; Kajos, M.; Venables, D.; Ruuskanen, T.; Levula, J.; et al. Enhanced Volatile Organic Compounds Emissions and Organic Aerosol Mass Increase the Oligomer Content of Atmospheric Aerosols. Sci. Rep. 2016, 6 (1), 35038.
- (18) Ng, N. L.; Brown, S. S.; Archibald, A. T.; Atlas, E.; Cohen, R. C.; Crowley, J. N.; Day, D. A.; Donahue, N. M.; Fry, J. L.; Fuchs, H.; et al. Nitrate Radicals and Biogenic Volatile Organic Compounds: Oxidation, Mechanisms, and Organic Aerosol. *Atmos. Chem. Phys.* **2017**, *17* (3), 2103–2162.
- (19) Pye, H. O. T.; Chan, A. W. H.; Barkley, M. P.; Seinfeld, J. H. Global Modeling of Organic Aerosol: The Importance of Reactive Nitrogen (NO<sub>x</sub> and NO<sub>3</sub>). *Atmos. Chem. Phys.* **2010**, *10* (22), 11261–11276.
- (20) Hoyle, C. R.; Berntsen, T.; Myhre, G.; Isaksen, I. S. A. Secondary Organic Aerosol in the Global Aerosol Chemical Transport Model Oslo CTM2. *Atmos. Chem. Phys.* **2007**, *7* (21), 5675–5694.
- (21) Ayres, B. R.; Allen, H. M.; Draper, D. C.; Brown, S. S.; Wild, R. J.; Jimenez, J. L.; Day, D. A.; Campuzano-Jost, P.; Hu, W.; de Gouw, J.; et al. Organic Nitrate Aerosol Formation via NO<sub>3</sub> + BVOC in the Southeastern US. *Atmos. Chem. Phys.* **2015**, *15* (23), 13377–13392.
- (22) Xu, L.; Suresh, S.; Guo, H.; Weber, R. J.; Ng, N. L. Aerosol Characterization over the Southeastern United States Using High Resolution Aerosol Mass Spectrometry: Spatial and Seasonal Variation of Aerosol Composition, Sources, and Organic Nitrates. *Atmos. Chem. Phys.* **2015**, *15* (13), 7307–7336.
- (23) Pye, H. O. T.; Luecken, D. J.; Xu, L.; Boyd, C. M.; Ng, N. L.; Baker, K. R.; Ayres, B. R.; Bash, J. O.; Baumann, K.; Carter, W. P. L.; et al. Modeling the Current and Future Roles of Particulate Organic Nitrates in the Southeastern United States. *Environ. Sci. Technol.* **2015**, 49 (24), 14195–14203.
- (24) Hallquist, M.; Wängberg, I.; Ljungström, E.; Barnes, I.; Becker, K.-H. Aerosol and Product Yields from NO<sub>3</sub> Radical-Initiated Oxidation of Selected Monoterpenes. *Environ. Sci. Technol.* **1999**, 33 (4), 553–559.
- (25) Bonn, B.; Moorgat, G. K. New Particle Formation during alphaand beta-Pinene Oxidation by O<sub>3</sub>, OH and NO<sub>3</sub>, and the Influence of Water Vapour: Particle Size Distribution Studies. *Atmos. Chem. Phys.* **2002**, 2 (3), 183–196.
- (26) Spittler, M.; Barnes, I.; Bejan, I.; Brockmann, K. J.; Benter, Th.; Wirtz, K. Reactions of NO<sub>3</sub> Radicals with Limonene and  $\alpha$ -Pinene: Product and SOA Formation. *Atmos. Environ.* **2006**, *40*, 116–127.
- (27) Perraud, V.; Bruns, E. A.; Ezell, M. J.; Johnson, S. N.; Greaves, J.; Finlayson-Pitts, B. J. Identification of Organic Nitrates in the NO<sub>3</sub> Radical Initiated Oxidation of  $\alpha$ -Pinene by Atmospheric Pressure Chemical Ionization Mass Spectrometry. *Environ. Sci. Technol.* **2010**, 44 (15), 5887–5893.
- (28) Fry, J. L.; Draper, D. C.; Barsanti, K. C.; Smith, J. N.; Ortega, J.; Winkler, P. M.; Lawler, M. J.; Brown, S. S.; Edwards, P. M.; Cohen, R. C.; et al. Secondary Organic Aerosol Formation and Organic Nitrate Yield from NO<sub>3</sub> Oxidation of Biogenic Hydrocarbons. *Environ. Sci. Technol.* **2014**, 48 (20), 11944–11953.
- (29) Nah, T.; Sanchez, J.; Boyd, C. M.; Ng, N. L. Photochemical Aging of  $\alpha$ -Pinene and  $\beta$ -Pinene Secondary Organic Aerosol Formed from Nitrate Radical Oxidation. *Environ. Sci. Technol.* **2016**, *50* (1), 222–231.
- (30) Berkemeier, T.; Takeuchi, M.; Eris, G.; Ng, N. L. Kinetic Modeling of Formation and Evaporation of Secondary Organic Aerosol from NO<sub>3</sub> Oxidation of Pure and Mixed Monoterpenes. *Atmos. Chem. Phys.* **2020**, 20 (24), 15513–15535.
- (31) Bates, K. H.; Burke, G. J. P.; Cope, J. D.; Nguyen, T. B. The Nitrate Radical (NO<sub>3</sub>) Oxidation of Alpha-Pinene Is a Significant Source of Secondary Organic Aerosol and Organic Nitrogen under Simulated Ambient Nighttime Conditions. *Atmos. Chem. Phys.* **2022**, 22, 1467–1482.

- (32) Hatakeyama, S.; Izumi, K.; Fukuyama, T.; Akimoto, H.; Washida, N. Reactions of OH with  $\alpha$ -Pinene and  $\beta$ -Pinene in Air: Estimate of Global CO Production from the Atmospheric Oxidation of Terpenes. *J. Geophys. Res. Atmospheres* **1991**, 96 (D1), 947–958.
- (33) Kroll, J. H.; Seinfeld, J. H. Chemistry of Secondary Organic Aerosol: Formation and Evolution of Low-Volatility Organics in the Atmosphere. *Atmos. Environ.* **2008**, *42* (16), 3593–3624.
- (34) Orlando, J. J.; Tyndall, G. S. Laboratory Studies of Organic Peroxy Radical Chemistry: An Overview with Emphasis on Recent Issues of Atmospheric Significance. *Chem. Soc. Rev.* **2012**, *41* (19), 6294
- (35) Ziemann, P. J.; Atkinson, R. Kinetics, Products, and Mechanisms of Secondary Organic Aerosol Formation. *Chem. Soc. Rev.* **2012**, *41* (19), 6582.
- (36) Ehn, M.; Thornton, J. A.; Kleist, E.; Sipilä, M.; Junninen, H.; Pullinen, I.; Springer, M.; Rubach, F.; Tillmann, R.; Lee, B.; et al. A Large Source of Low-Volatility Secondary Organic Aerosol. *Nature* **2014**, *506* (7489), 476–479.
- (37) Kirchner, F.; Stockwell, W. Effect of Peroxy Radical Reactions on the Predicted Concentrations of Ozone, Nitrogenous Compounds, and Radicals. *J. Geophys. Res. Atmospheres* **1996**, *101*, 21007–21022.
- (38) Mao, J.; Ren, X.; Zhang, L.; Van Duin, D. M.; Cohen, R. C.; Park, J.-H.; Goldstein, A. H.; Paulot, F.; Beaver, M. R.; Crounse, J. D.; et al. Insights into Hydroxyl Measurements and Atmospheric Oxidation in a California Forest. *Atmos. Chem. Phys.* **2012**, *12* (17), 8009–8020.
- (39) Boyd, C. M.; Sanchez, J.; Xu, L.; Eugene, A. J.; Nah, T.; Tuet, W. Y.; Guzman, M. I.; Ng, N. L. Secondary Organic Aerosol Formation from the  $\beta$ -Pinene+NO<sub>3</sub> System: Effect of Humidity and Peroxy Radical Fate. *Atmos. Chem. Phys.* **2015**, *15* (13), 7497–7522.
- (40) Schwantes, R. H.; Teng, A. P.; Nguyen, T. B.; Coggon, M. M.; Crounse, J. D.; St. Clair, J. M.; Zhang, X.; Schilling, K. A.; Seinfeld, J. H.; Wennberg, P. O. Isoprene NO<sub>3</sub> Oxidation Products from the RO<sub>2</sub> + HO<sub>2</sub> Pathway. *J. Phys. Chem. A* **2015**, *119* (40), 10158–10171.
- (41) Takeuchi, M.; Ng, N. L. Chemical Composition and Hydrolysis of Organic Nitrate Aerosol Formed from Hydroxyl and Nitrate Radical Oxidation of  $\alpha$  -Pinene and  $\beta$  -Pinene. *Atmos. Chem. Phys.* **2019**, *19* (19), 12749–12766.
- (42) Berndt, T.; Scholz, W.; Mentler, B.; Fischer, L.; Herrmann, H.; Kulmala, M.; Hansel, A. Accretion Product Formation from Self- and Cross-Reactions of RO<sub>2</sub> Radicals in the Atmosphere. *Angew. Chem., Int. Ed.* **2018**, *57* (14), 3820–3824.
- (43) Claflin, M. S.; Ziemann, P. J. Identification and Quantitation of Aerosol Products of the Reaction of  $\beta$ -Pinene with NO $_3$  Radicals and Implications for Gas- and Particle-Phase Reaction Mechanisms. *J. Phys. Chem. A* **2018**, *122* (14), 3640–3652.
- (44) DeVault, M. P.; Ziemann, P. J. Gas- and Particle-Phase Products and Their Mechanisms of Formation from the Reaction of  $\Delta$ -3-Carene with NO $_3$  Radicals. *J. Phys. Chem. A* **2021**, 125 (47), 10207–10222.
- (45) DeVault, M. P.; Ziola, A. C.; Ziemann, P. J. Products and Mechanisms of Secondary Organic Aerosol Formation from the NO<sub>3</sub> Radical-Initiated Oxidation of Cyclic and Acyclic Monoterpenes. *Earth Space Chem.* **2022**, *6* (8), 2076–2092.
- (46) Krechmer, J. E.; Pagonis, D.; Ziemann, P. J.; Jimenez, J. L. Quantification of Gas-Wall Partitioning in Teflon Environmental Chambers Using Rapid Bursts of Low-Volatility Oxidized Species Generated in Situ. *Environ. Sci. Technol.* **2016**, *50* (11), 5757–5765.
- (47) Krechmer, J. E.; Day, D. A.; Ziemann, P. J.; Jimenez, J. L. Direct Measurements of Gas/Particle Partitioning and Mass Accommodation Coefficients in Environmental Chambers. *Environ. Sci. Technol.* **2017**, *51* (20), 11867–11875.
- (48) Dubé, W. P.; Brown, S. S.; Osthoff, H. D.; Nunley, M. R.; Ciciora, S. J.; Paris, M. W.; McLaughlin, R. J.; Ravishankara, A. R. Aircraft Instrument for Simultaneous, in Situ Measurement of  $NO_3$  and  $N_2O_5$  via Pulsed Cavity Ring-down Spectroscopy. *Rev. Sci. Instrum.* 2006, 77 (3), 034101.
- (49) Wagner, N. L.; Dubé, W. P.; Washenfelder, R. A.; Young, C. J.; Pollack, I. B.; Ryerson, T. B.; Brown, S. S. Diode Laser-Based Cavity

- Ring-down Instrument for NO<sub>3</sub>, N<sub>2</sub>O<sub>5</sub>, NO, NO<sub>2</sub> and O<sub>3</sub> from Aircraft. *Atmos. Meas. Tech.* **2011**, 4 (6), 1227–1240.
- (50) Algrim, L. B.; Ziemann, P. J. Effect of the Keto Group on Yields and Composition of Organic Aerosol Formed from OH Radical-Initiated Reactions of Ketones in the Presence of NO<sub>x</sub>. J. Phys. Chem. A **2016**, 120 (35), 6978–6989.
- (51) DeCarlo, P. F.; Kimmel, J. R.; Trimborn, A.; Northway, M. J.; Jayne, J. T.; Aiken, A. C.; Gonin, M.; Fuhrer, K.; Horvath, T.; Docherty, K. S.; et al. Field-Deployable, High-Resolution, Time-of-Flight Aerosol Mass Spectrometer. *Anal. Chem.* **2006**, 78 (24), 8281–8289.
- (52) Canagaratna, M. R.; Jayne, J. T.; Jimenez, J. L.; Allan, J. D.; Alfarra, M. R.; Zhang, Q.; Onasch, T. B.; Drewnick, F.; Coe, H.; Middlebrook, A.; et al. Chemical and Microphysical Characterization of Ambient Aerosols with the Aerodyne Aerosol Mass Spectrometer. *Mass Spectrom. Rev.* 2007, 26 (2), 185–222.
- (53) Sueper, D. https://cires1.colorado.edu/jimenez-group/ToFAMSResources/ToFSoftware/, 2021.
- (54) Jimenez, J. L.; Canagaratna, M. R.; Drewnick, F.; Allan, J. D.; Alfarra, M. R.; Middlebrook, A. M.; Slowik, J. G.; Zhang, Q.; Coe, H.; Jayne, J. T.; et al. Comment on "The Effects of Molecular Weight and Thermal Decomposition on the Sensitivity of a Thermal Desorption Aerosol Mass Spectrometer". *Aerosol Sci. Technol.* **2016**, *50* (9), i—xv.
- (55) Xu, W.; Lambe, A.; Silva, P.; Hu, W.; Onasch, T.; Williams, L.; Croteau, P.; Zhang, X.; Renbaum-Wolff, L.; Fortner, E.; et al. Laboratory Evaluation of Species-Dependent Relative Ionization Efficiencies in the Aerodyne Aerosol Mass Spectrometer. *Aerosol Sci. Technol.* **2018**, 52 (6), 626–641.
- (56) Canagaratna, M. R.; Jimenez, J. L.; Kroll, J. H.; Chen, Q.; Kessler, S. H.; Massoli, P.; Hildebrandt Ruiz, L.; Fortner, E.; Williams, L. R.; Wilson, K. R.; et al. Elemental Ratio Measurements of Organic Compounds Using Aerosol Mass Spectrometry: Characterization, Improved Calibration, and Implications. *Atmos. Chem. Phys.* **2015**, *15* (1), 253–272.
- (57) Day, D. A.; Campuzano-Jost, P.; Nault, B. A.; Palm, B. B.; Hu, W.; Guo, H.; Wooldridge, P. J.; Cohen, R. C.; Docherty, K. S.; Huffman, J. A.; et al. A Systematic Re-Evaluation of Methods for Quantification of Bulk Particle-Phase Organic Nitrates Using Real-Time Aerosol Mass Spectrometry. *Atmos. Meas. Tech.* **2022**, *15*, 459–483.
- (58) Keehan, N. I.; Brownwood, B.; Marsavin, A.; Day, D. A.; Fry, J. L. A Thermal-Dissociation—Cavity Ring-down Spectrometer (TD-CRDS) for the Detection of Organic Nitrates in Gas and Particle Phases. *Atmos. Meas. Tech.* **2020**, *13* (11), 6255—6269.
- (59) Eisele, F. L.; Tanner, D. J. Measurement of the Gas Phase Concentration of H2SO4 and Methane Sulfonic Acid and Estimates of  $\rm H_2SO_4$  Production and Loss in the Atmosphere. *J. Geophys. Res. Atmospheres* **1993**, 98 (D5), 9001–9010.
- (60) Sinclair, D.; La Mer, V. K. Light Scattering as a Measure of Particle Size in Aerosols. The Production of Monodisperse Aerosols. *Chem. Rev.* **1949**, *44* (2), 245–267.
- (61) von der Weiden, S.-L.; Drewnick, F.; Borrmann, S. Particle Loss Calculator a New Software Tool for the Assessment of the Performance of Aerosol Inlet Systems. *Atmos. Meas. Tech.* **2009**, 2 (2), 479–494
- (62) Kuwata, M.; Zorn, S. R.; Martin, S. T. Using Elemental Ratios to Predict the Density of Organic Material Composed of Carbon, Hydrogen, and Oxygen. *Environ. Sci. Technol.* **2012**, *46* (2), 787–794.
- (63) Liu, X.; Day, D. A.; Krechmer, J. E.; Brown, W.; Peng, Z.; Ziemann, P. J.; Jimenez, J. L. Direct Measurements of Semi-Volatile Organic Compound Dynamics Show near-Unity Mass Accommodation Coefficients for Diverse Aerosols. *Commun. Chem.* **2019**, 2 (1), 1–9.
- (64) Peng, Z.; Jimenez, J. L. KinSim: A Research-Grade, User-Friendly, Visual Kinetics Simulator for Chemical-Kinetics and Environmental-Chemistry Teaching. *J. Chem. Educ.* **2019**, *96* (4), 806–811.
- (65) Draper, D. C.; Myllys, N.; Hyttinen, N.; Møller, K. H.; Kjaergaard, H. G.; Fry, J. L.; Smith, J. N.; Kurtén, T. Formation of

- Highly Oxidized Molecules from  $NO_3$  Radical Initiated Oxidation of  $\Delta$ -3-Carene: A Mechanistic Study. ACS Earth Space Chem. **2019**, 3 (8), 1460–1470.
- (66) Kurtén, T.; Møller, K. H.; Nguyen, T. B.; Schwantes, R. H.; Misztal, P. K.; Su, L.; Wennberg, P. O.; Fry, J. L.; Kjaergaard, H. G. Alkoxy Radical Bond Scissions Explain the Anomalously Low Secondary Organic Aerosol and Organonitrate Yields From  $\alpha$ -Pinene + NO<sub>3</sub>. *J. Phys. Chem. Lett.* **2017**, 8 (13), 2826–2834.
- (67) Jenkin, M. E.; Valorso, R.; Aumont, B.; Rickard, A. R. Estimation of Rate Coefficients and Branching Ratios for Reactions of Organic Peroxy Radicals for Use in Automated Mechanism Construction. *Atmos. Chem. Phys.* **2019**, *19* (11), 7691–7717.
- (68) Crounse, J. D.; Nielsen, L. B.; Jørgensen, S.; Kjaergaard, H. G.; Wennberg, P. O. Autoxidation of Organic Compounds in the Atmosphere. J. Phys. Chem. Lett. 2013, 4 (20), 3513–3520.
- (69) Knap, H. C.; Jørgensen, S.; Kjaergaard, H. G. Theoretical Investigation of the Hydrogen Shift Reactions in Peroxy Radicals Derived from the Atmospheric Decomposition of 3-Methyl-3-Buten-1-Ol (MBO331. *Chem. Phys. Lett.* **2015**, *619*, 236–240.
- (70) Carlton, A. G.; de Gouw, J.; Jimenez, J. L.; Ambrose, J. L.; Attwood, A. R.; Brown, S.; Baker, K. R.; Brock, C.; Cohen, R. C.; Edgerton, S.; et al. Synthesis of the Southeast Atmosphere Studies: Investigating Fundamental Atmospheric Chemistry Questions. *Bull. Am. Meteorol. Soc.* **2018**, 99 (3), 547–567.
- (71) Faloona, I. C.; Tan, D.; Lesher, R. L.; Hazen, N. L.; Frame, C. L.; Simpas, J. B.; Harder, H.; Martinez, M.; Di Carlo, P.; Ren, X. A Laser-Induced Fluorescence Instrument for Detecting Tropospheric OH and  $\mathrm{HO}_2$ : Characteristics and Calibration. *J. Atmospheric Chem.* **2004**, *47*, 139–167.
- (72) Feiner, P. A.; Brune, W. H.; Miller, D. O.; Zhang, L.; Cohen, R. C.; Romer, P. S.; Goldstein, A. H.; Keutsch, F. N.; Skog, K. M.; Wennberg, P. O.; et al. Testing Atmospheric Oxidation in an Alabama Forest. *J. Atmospheric Sci.* **2016**, 73 (12), 4699–4710.
- (73) DeVault, M. P.; Ziemann, P. J. Gas- and Particle-Phase Products and Their Mechanisms of Formation from the Reaction of  $\Delta$ -3-Carene with NO<sub>3</sub> Radicals. *J. Phys. Chem. A* **2021**, 125 (47), 10207–10222.
- (74) Farmer, D. K.; Matsunaga, A.; Docherty, K. S.; Surratt, J. D.; Seinfeld, J. H.; Ziemann, P. J.; Jimenez, J. L. Response of an Aerosol Mass Spectrometer to Organonitrates and Organosulfates and Implications for Atmospheric Chemistry. *Proc. Natl. Acad. Sci. U. S. A.* 2010, 107 (15), 6670–6675.
- (75) Bahreini, R.; Ervens, B.; Middlebrook, A. M.; Warneke, C.; de Gouw, J. A.; DeCarlo, P. F.; Jimenez, J. L.; Brock, C. A.; Neuman, J. A.; Ryerson, T. B. Organic Aerosol Formation in Urban and Industrial Plumes near Houston and Dallas, Texas. *J. Geophys. Res. Atmospheres* **2009**, *114*, D00F16.
- (76) Takeuchi, M.; Wang, Y.; Nault, B. A.; Canagaratna, M.; Ng, N. L. N. Potential Underestimation of Particulate Organic Nitrate Concentration by an Aerosol Mass Spectrometer. (presentation). In American Association for Aerosol Research 39th Annual Conference (Virtual), Abstract No. 221, Oct 2021. Available from: https://aaarabstracts.com/2021/viewabstract.php?pid=221.
- (77) Shilling, J. E.; Chen, Q.; King, S. M.; Rosenoern, T.; Kroll, J. H.; Worsnop, D. R.; DeCarlo, P. F.; Aiken, A. C.; Sueper, D.; Jimenez, J. L.; et al. Loading-Dependent Elemental Composition of α-Pinene SOA Particles. *Atmos Chem. Phys.* **2009**, *9*, 771–782.
- (78) Shrivastava, M.; Cappa, C. D.; Fan, J.; Goldstein, A. H.; Guenther, A. B.; Jimenez, J. L.; Kuang, C.; Laskin, A.; Martin, S. T.; Ng, N. L.; et al. Recent Advances in Understanding Secondary Organic Aerosol: Implications for Global Climate Forcing: Advances in Secondary Organic Aerosol. Rev. Geophys. 2017, 55 (2), 509–559.
- (79) Ng, N. L.; Kwan, A. J.; Surratt, J. D.; Chan, A. W. H.; Chhabra, P. S.; Sorooshian, A.; Pye, H. O. T.; Crounse, J. D.; Wennberg, P. O.; Flagan, R. C.; et al. Secondary Organic Aerosol (SOA) Formation from Reaction of Isoprene with Nitrate Radicals (NO<sub>3</sub>). *Atmos. Chem. Phys.* **2008**, *8*, 4117–4140.
- (80) Xu, L.; Kollman, M. S.; Song, C.; Shilling, J. E.; Ng, N. L. Effects of NO<sub>x</sub> on the Volatility of Secondary Organic Aerosol from

Isoprene Photooxidation. Environ. Sci. Technol. 2014, 48 (4), 2253–2262.

- (81) Madronich, S.; Calvert, J. G. Permutation Reactions of Organic Peroxy Radicals in the Troposphere. *J. Geophys. Res. Atmospheres* **1990**, 95 (D5), 5697–5715.
- (82) Tyndall, G. S.; Cox, R. A.; Granier, C.; Lesclaux, R.; Moortgat, G. K.; Pilling, M. J.; Ravishankara, A. R.; Wallington, T. J. Atmospheric Chemistry of Small Organic Peroxy Radicals. *J. Geophys. Res. Atmospheres* **2001**, *106* (D11), 12157–12182.
- (83) Atkinson, R.; Baulch, D. L.; Cox, R. A.; Crowley, J. N.; Hampson, R. F.; Hynes, R. G.; Jenkin, M. E.; Rossi, M. J.; Troe, J. Evaluated Kinetic and Photochemical Data for Atmospheric Chemistry: Volume II Gas Phase Reactions of Organic Species. *Atmos. Chem. Phys.* **2006**, *6* (11), 3625–4055.
- (84) Kwan, A. J.; Chan, A. W. H.; Ng, N. L.; Kjaergaard, H. G.; Seinfeld, J. H.; Wennberg, P. O. Peroxy Radical Chemistry and OH Radical Production during the NO<sub>3</sub> -Initiated Oxidation of Isoprene. *Atmos. Chem. Phys.* **2012**, *12* (16), 7499–7515.
- (85) Bell, D. M.; Wu, C.; Bertrand, A.; Graham, E.; Schoonbaert, J.; Giannoukos, S.; Baltensperger, U.; Prevot, A. S. H.; Riipinen, I.; El Haddad, I.; Mohr, C. Particle-Phase Processing of α-Pinene NO<sub>3</sub> Secondary Organic Aerosol in the Dark. *Atmos. Chem. Phys.* **2022**, DOI: 10.5194/acp-2021-379.
- (86) Jenkin, M. E.; Hurley, M. D.; Wallington, T. J. Investigation of the Radical Product Channel of the CH<sub>3</sub>COO<sub>2</sub> + HO<sub>2</sub> Reaction in the Gas Phase. *Phys. Chem. Chem. Phys. PCCP* **2007**, 9 (24), 3149–3162.
- (87) Dillon, T. J.; Crowley, J. N. Direct Detection of OH Formation in the Reactions of HO<sub>2</sub> with CH<sub>3</sub>C(O)O<sub>2</sub> and Other Substituted Peroxy Radicals. *Atmos. Chem. Phys.* **2008**, *8* (16), 4877–4889.
- (88) Hasson, A. S.; Kuwata, K. T.; Arroyo, M. C.; Petersen, E. B. Theoretical Studies of the Reaction of Hydroperoxy Radicals (HO<sub>2</sub>) with Ethyl Peroxy (CH<sub>3</sub>CH<sub>2</sub>O<sub>2</sub>), Acetyl Peroxy (CH<sub>3</sub>C(O)O<sub>2</sub>), and Acetonyl Peroxy (CH<sub>3</sub>C(O)CH<sub>2</sub>O<sub>2</sub>) Radicals. *J. Photochem. Photobiol. Chem.* **2005**, 176 (1–3), 218–230.
- (89) Jokinen, T.; Sipilä, M.; Richters, S.; Kerminen, V.-M.; Paasonen, P.; Stratmann, F.; Worsnop, D.; Kulmala, M.; Ehn, M.; Herrmann, H.; et al. T. Rapid Autoxidation Forms Highly Oxidized RO<sub>2</sub> Radicals in the Atmosphere. *Angew. Chem., Int. Ed.* **2014**, *53* (52), 14596–14600.
- (90) Dam, M.; Draper, D. C.; Marsavin, A.; Fry, J. L.; Smith, J. N. Observations of Gas-Phase Products from the Nitrate-Radical-Initiated Oxidation of Four Monoterpenes. *Atmos. Chem. Phys.* **2022**, 22 (13), 9017–9031.
- (91) Pagonis, D.; Ziemann, P. J. Chemistry of Hydroperoxycarbonyls in Secondary Organic Aerosol. *Aerosol Sci. Technol.* **2018**, 52 (10), 1178–1193.
- (92) Claflin, M. S.; Krechmer, J. E.; Hu, W.; Jimenez, J. L.; Ziemann, P. J. Functional Group Composition of Secondary Organic Aerosol Formed from Ozonolysis of  $\alpha$ -Pinene Under High VOC and Autoxidation Conditions. *ACS Earth Space Chem.* **2018**, 2 (11), 1196–1210.
- (93) Pankow, J. F.; Asher, W. E. SIMPOL.1: A Simple Group Contribution Method for Predicting Vapor Pressures and Enthalpies of Vaporization of Multifunctional Organic Compounds. *Atmos. Chem. Phys.* **2008**, 8 (10), 2773–2796.
- (94) Kim, S.; Wolfe, G. M.; Mauldin, L.; Cantrell, C.; Guenther, A.; Karl, T.; Turnipseed, A.; Greenberg, J.; Hall, S. R.; Ullmann, K.; et al. Evaluation of  $HO_x$  Sources and Cycling Using Measurement-Constrained Model Calculations in a 2-Methyl-3-Butene-2-Ol (MBO) and Monoterpene (MT) Dominated Ecosystem. *Atmos. Chem. Phys.* **2013**, *13* (4), 2031–2044.
- (95) Fry, J. L.; Draper, D. C.; Zarzana, K. J.; Campuzano-Jost, P.; Day, D. A.; Jimenez, J. L.; Brown, S. S.; Cohen, R. C.; Kaser, L.; Hansel, A.; et al. Observations of Gas- and Aerosol-Phase Organic Nitrates at BEACHON-Rombas 2011. *Atmos. Chem. Phys.* **2013**, *13* (17), 8585–8605.
- (96) Shen, H.; Zhao, D.; Pullinen, I.; Kang, S.; Vereecken, L.; Fuchs, H.; Acir, I.-H.; Tillmann, R.; Rohrer, F.; Wildt, J.; et al. Highly

Oxygenated Organic Nitrates Formed from NO<sub>3</sub> Radical-Initiated Oxidation of  $\beta$ -Pinene. *Environ. Sci. Technol.* **2021**, *55*, 15658–15671. (97) Geron, C.; Rasmussen, R.; R. Arnts, R.; Guenther, A. A Review and Synthesis of Monoterpene Speciation from Forests in the United States. *Atmos. Environ.* **2000**, *34* (11), 1761–1781.

# **□** Recommended by ACS

Chemistry of Secondary Organic Aerosol Formation from Reactions of Monoterpenes with OH Radicals in the Presence of  $NO_{\nu}$ 

Marla P. DeVault, Paul J. Ziemann, et al.

OCTOBER 17, 2022

THE JOURNAL OF PHYSICAL CHEMISTRY A

DEAD E

Products and Mechanisms of Secondary Organic Aerosol Formation from the NO<sub>3</sub> Radical-Initiated Oxidation of Cyclic and Acyclic Monoterpenes

Marla P. DeVault, Paul J. Ziemann, et al.

JULY 26, 2022

ACS EARTH AND SPACE CHEMISTRY

READ 🗹

New Particle Formation and Growth Dynamics for  $\alpha$ -Pinene Ozonolysis in a Smog Chamber and Implications for Ambient Environments

Ching-Wei Chu, Hui-Ming Hung, et al.

NOVEMBER 22, 2022

ACS EARTH AND SPACE CHEMISTRY

READ 🗹

Gas-Particle Partitioning and SOA Yields of Organonitrate Products from NO<sub>3</sub>-Initiated Oxidation of Isoprene under Varied Chemical Regimes

Bellamy Brownwood, Juliane L. Fry, et al.

MARCH 11, 2021

ACS EARTH AND SPACE CHEMISTRY

READ 🗹

Get More Suggestions >